# Assessing the effective spatial characteristics of input features through physics-informed machine learning models in inundation forecasting during typhoons

Bing-Chen Jhong, Chung-Yi Lin, You-Da Jhong, Hsiang-Kuan Chang, Jung-Lien Chu & Hsi-Ting Fang

View supplementary material

Published online: 19 Jul 2022.

Submit your article to this journal

Article views: 58

View related articles

View Crossmark data

IAHS AISH

Taylor & Francis
Taylor & Francis Group

Check for updates

# Assessing the effective spatial characteristics of input features through physics-informed machine learning models in inundation forecasting during typhoons

Bing-Chen Jhong [iD][a], Chung-Yi Lin[b], You-Da Jhong[c], Hsiang-Kuan Chang[d], Jung-Lien Chu[e] and Hsi-Ting Fang[f]

[a]Department of Civil and Construction Engineering, National Taiwan University of Science and Technology, Taipei, Taiwan; [b]Department of Civil and Environmental Engineering, Lehigh University, Bethlehem, PA, USA; [c]College of Engineering and Science, Feng Chia University, Taichung, Taiwan; [d]Center for Weather Climate and Disaster Research, National Taiwan University, Taipei, Taiwan; [e]Meteorology Division, National Science and Technology Center for Disaster Reduction, Taipei, Taiwan; [f]Department of Hydraulic Engineering, Taiwan Integrated Disaster Prevention of Technology Engineering Consulting Co., Ltd, Taipei, Taiwan

**ABSTRACT**

This study aimed to assess the effective spatial characteristics of input features by using physics-informed, machine learning (ML)-based inundation forecasting models. To achieve this aim, inundation depth data were simulated using a numerical hydrodynamic model to obtain training and testing data for these ML-based models. Effective spatial information was identified using a back-propagation neural network, an adaptive neuro-fuzzy inference system, support vector machine, and a hybrid model combining support vector machine and a multi-objective genetic algorithm. The conventional average rainfall determined using the Thiessen polygon method, raingauge observations, radar-based rainfall data, and typhoon characteristics were used as the inputs of the aforementioned ML models. These models were applied in inundation forecasting for Yilan County, Taiwan, and the hybrid model had the best forecasting performance. The results show that the hybrid model with crucial features and appropriate lag lengths gave the best performance.

## 1 Introduction

Tropical cyclones are highly destructive. The torrential rain induced by tropical cyclones yields water resources, especially for island regions and countries. However, this heavy rain leads to flood inundation, which can cause considerable economic loss, property damage, and human deaths as well as negatively affecting agricultural environments. Taiwan is located in the main path of western North Pacific typhoons (i.e. mature tropical cyclones developing in the northwestern Pacific Ocean). During the past 100 years, Taiwan has been hit by an average of three to four typhoons annually. To mitigate the harmful effects of inundation on human life and property, early warning systems, which are designed to increase preparation time, have been developed. Accurate forecasts of the weather and inundation depth are critical for emergency evacuations. Therefore, improving inundation forecasting (IF) is crucial for establishing an effective disaster warning system.

The accurate forecasting of hourly inundation depth during typhoons is challenging. With advances in numerical modelling and computing techniques, two-dimensional (2D) numerical hydrodynamic models have been extensively used for the simulation of the complex physical processes underlying flood dynamics. Moreover, a database of pre-modelled flood extents can be used to simulate the aforementioned processes for disaster management (Henonin *et al.* 2013, René *et al.* 2014,

Bhola *et al.* 2018). However, the aforementioned methods have some serious limitations, such as their high computational, personnel, and data storage requirements (for inundation database preparation and management). The use of the complex models of physical processes for real-time IF is difficult. Furthermore, inundation scenarios might become antiquated because of changing environmental factors, such as topography, land use, and engineering facilities. Inundation databases must be constantly updated with new simulations.

A modelling method with a low computational load should be developed to overcome the technical challenges associated with real-time IF. Machine learning (ML) approaches, which can effectively capture complex nonlinear relationships between inputs and output, are alternatives to 2D numerical models, which are inefficient in real-time forecasting. ML methods have been increasingly applied to IF, and these models have been based on back-propagation neural networks (BPNNs; Chang *et al.* 2010, 2014a, Pan *et al.* 2011, Jhong *et al.* 2016), adaptive neuro-fuzzy inference systems (ANFISs; Ouyang 2017), support vector machine (SV; Lin *et al.* 2013, Jhong *et al.* 2016, 2017), nonlinear autoregressive networks with exogenous inputs (NARXs; Chang *et al.* 2014a), and recurrent NARXs (Shen and Chang 2013, Chang *et al.* 2014b). The literature on this topic is summarized in Table 1. Several clustering-based methods, such as the *k*-means

**Table 1.** Literature summary on the topic of hourly real-time forecasting of inundation depth based on the application of machine-learning approaches and artificial neural networks.

| Paper | Study question | Model input | Model output | Algorithm components | Contributions |
|---|---|---|---|---|---|
| Chang et al. (2010) | How to provide forecasted information of flood inundation depth | (1) Current and antecedent rainfall observation of five nearby raingauges (2) Antecedent forecasting flood depths of the control points | 1-h-ahead flood depths | A clustering-based hybrid inundation model: (1) k-means method used to categorize the data points of flooding characteristics (2) BPNN for each control point (3) Linear regression models for other grids | Applied k-means clustering method and neural network approach to effectively generate a 1-h-ahead flood inundation map |
| Pan et al. (2011) | How to obtain real-time forecasting inundation information in lowland regions | (1) Present rainfall observation (2) Past 22-h rainfall observation (3) Present rainfall accumulation (4) Past 22-h rainfall accumulation | 1-h-ahead water depths for all representative inundation locations | A rainfall-inundation hybrid neural network (RiHNN): (1) Validate the 2-D overland-flow model (2) Select representative inundation locations (3) Build a synthetic potential inundation database (4) Construct the inundation forecasting model integrating PCA and BPNN | (1) Applied PCA to reduce the input neurons (2) Mass potential inundation maps generated based on real/synthetic rainfall events for training the forecasting model |
| Lin et al. (2013) | How to provide real-time regional inundation forecasting maps | (1) Inundation depth (2) Rainfall observation | 1- to 3-h lead time inundation maps | A regional inundation forecasting model: (1) k-means cluster analysis used to group the inundation depths and to identify the control points (2) SVM used for point forecasting module (3) Spatial expansion module was designed to expand the point forecasts to the spatial forecasts | Applied k-means clustering method and NN approaches to generate a 1- to 3-h-ahead flood inundation map |
| Shen and Chang (2013) | How to provide forecasted information of flood inundation depth | (1) Inundation depth (2) Rainfall observation | 1- to 6-h lead time forecasting of inundation depth | Applied R-NARX to forecast multistep-ahead inundation depths in an inundation area | Developed a R-NARX network to forecast multistep-ahead inundation depths |
| Chang et al. (2014a) | How to provide forecasted information of flood inundation depth | (1) Inundation depth (2) Rainfall observation | 1- to 6-h lead time forecasting water level at floodwater storage pond | (1) BPNN (2) Elman NN (3) NARX | (1) Compare different model structures along with the gamma test to select effective factors (2) Investigate the reliability and accuracy of short-term (10–60-min) forecast models for the floodwater storage pond of a sewer-pumping system |
| Chang et al. (2014b) | How to provide real-time regional inundation forecasting maps | (1) Inundation depth (2) Rainfall observation | 1-3-h lead time inundation maps | A hybrid SOM-R-NARX model: (1) configuring the SOM to categorize regional inundation maps into a meaningful topology (2) building an R-NARX to forecast the total inundated volume (3) adjusting the weights of the selected neuron in the SOM based on the forecasted total inundated volume to obtain a real-time adapted regional inundation map | Form a meaningful topology of inundation maps and real-time update the selected inundation map according to a forecasted total inundated volume |
| Jhong et al. (2016) | (1) How to provide forecasted information on flood inundation depth (2) How effective typhoon characteristics can improve the accuracy of forecasts of hourly inundation depths | (1) Inundation depth (2) Rainfall observation (3) Typhoon characteristics | 1- to 6-h time forecasting inundation depth | A new type of inundation forecasting model integrating SVM with MOGA, called MGSVM, compared to: (1) BPNN (2) SVM | By integrating SVM with MOGA, the proposed MGSVM model can improve the forecasting performance with the effective typhoon characteristics |
| Jhong et al. (2017) | How to provide real-time regional inundation forecasting maps | (1) Current inundation depth of the other grids (2) Forecasted inundation depth of the reference points (3) Rainfall observation | 1- to 6-h lead-time inundation maps during typhoons | An integrated two-stage SVM approach: (1) Point forecasting (2) Spatial expansion | Develop a two-stage inundation forecasting approach based on SVM and obtain reasonable forecasted inundation maps |
| Ouyang (2017) | How to investigate the characteristics of ANFIS models for typhoon inundation level forecasting | (1) Rainfall data (2) Water level data | 1-h lead-time inundation water level | Two types of ANFIS-based models: (1) ANFIS-N (2) ANFIS-R | The recursive and non-recursive types of models demonstrate superior performance on all the aspects inspected |

PCA: principal component analysis.

algorithm and self-organizing maps, have been frequently used to categorize inundation depths or data points (Chang *et al.* 2010, 2014b, Lin *et al.* 2013). Because of the importance of obtaining accurate inundation forecasts from early warning systems, most of the reviewed studies have focused on obtaining accurate forecasts of flood inundation depth (e.g. Chang *et al.* 2010, 2014a, Pan *et al.* 2011, Shen and Chang 2013, Jhong *et al.* 2016). In addition to the specific control points of inundation locations, reasonable levels of spatial inundation must be predicted to obtain inundation forecast maps (e.g. Lin *et al.* 2013, Chang *et al.* 2014b, Jhong *et al.* 2017).

In most cases, physics-based numerical models are constructed with as many input variables as possible. ML approaches can discover patterns and predict system behaviours to deliver data-driven solutions. As presented in Table 1, multiple variables, such as past and current inundation depths, rainfall observations, rainfall accumulation, and typhoon characteristics, are used as inputs of IF models. Several studies have input the mean rainfall observations calculated using the Thiessen method (e.g. Pan *et al.* 2011), data from few raingauges (e.g. Chang *et al.* 2010, Shen and Chang 2013), and data from many raingauges in a study region (e.g. Pan *et al.* 2014) into IF models. Nevertheless, little research has been conducted, first, on the objective and automatic identification of useful input features from multiple variables and from the lag lengths of each input and, second, on the analysis of spatial information from raingauge observations in catchments for IF during typhoons. These crucial aspects should be considered in the establishment of data-driven ML-based models. Moreover, when selecting an ML approach for IF, one should consider that the spatial and temporal variations of precipitation are primary factors affecting the hydrological response and thus the accuracy of IF (Versini 2012, Pan *et al.* 2014). Therefore, multiple input features comprising the effective spatial information from raingauges during typhoons should be evaluated to improve IF.

Jhong *et al.* (2016) developed an IF model by using a hybrid algorithm that is based on both SVM, which is a widely used data-driven approach, and the multi-objective genetic algorithm (MOGA), which is a commonly used optimization algorithm in ML-based approaches (Yadav and Satyannarayana 2020), to optimize multiple input features with high accuracy. This hybrid algorithm (hereinafter referred to as the SVM-MOGA) has been successfully applied to hourly typhoon rainfall forecasting (Lin and Jhong 2015), spatial–temporal groundwater level forecasting (Fang *et al.* 2019), and half-hourly suspended sediment concentration prediction (Huang *et al.* 2019). Although the aforementioned studies have indicated the advantages of integrating SVM and the MOGA, few studies have compared the accuracy of SVM-MOGA-based models and conventional ML-based models, such as BPNNs, ANFISs, and SVM, on applying rainfall observations obtained from raingauges in a watershed and radar-based rainfall data as inputs of the SVM-MOGA-based models and on optimizing effective rainfall observations and their appropriate input lag lengths as compared with the improvement of the conventional average rainfall obtained using the Thiessen method. The determination of the lag lengths of crucial inputs is one of the most important steps in ML modelling. The lag lengths of various inputs affect the forecasting capability of ML-based

models because of the effect of the time of concentration in the study area. Therefore, we propose a physics-informed ML model based on the SVM-MOGA to assess the effective spatial characteristics of input features.

This study had the following three objectives: (1) to investigate critical input variables for IF, (2) to conduct spatial analysis of raingauge observations in various regions, and (3) to determine appropriate lag lengths of each input variable at different lead times. The proposed model was applied to IF for Yilan County, Taiwan, to demonstrate its advantages. The rest of this paper is organized as follows. The methods used in this study are introduced in Section 2. The adopted materials and the background of the study area are described in Section 3. Section 4 presents the results of model comparisons and describes the identification of effective input variables and appropriate lag lengths in different regions. The influences of the addition of typhoon characteristics and the spatial information of the optimized input features on the proposed model are discussed in Section 5. Finally, Section 6 concludes this study.

## 2 Methodology

### 2.1 Back-propagation neural networks

Rumelhart *et al.* (1986) were the first to develop a BPNN, which is the most popular type of neural network. A BPNN contains a supervised multilayer feedforward neural network that uses the back-propagation algorithm for network training. BPNNs comprise three layers in most cases: an input layer, a hidden layer, and an output layer. In the input layer, the input variables $x_i (i = 1, 2, \ldots, n)$ are neurons, and $\hat{y}_j (j = 1, 2, \ldots, q)$ are the output variables of the $j$th neuron in the output layer. The output $\hat{y}_j$ is expected to fit the actual (target) output $y_j$. A BPNN with $h$ neurons in the hidden layer can be expressed as follows:

$$\hat{y}_j = \sum_{k=1}^{h} w_{kj} \cdot G\left(\sum_{i=1}^{n} w_{ik} \cdot x_i + b_k\right) + c_j \quad (1)$$

where $w_{ik}$ denotes the weight linking the $i$th neuron in the input layer to the $k$th neuron in the hidden layer, $w_{kj}$ is the weight linking the $k$th neuron in the hidden layer to the $j$th neuron in the output layer, $b_k$ is the bias of the $k$th hidden neuron, $c_j$ is the bias of the $j$th output neuron, and $G()$ represents the activation function of the hidden neuron. In general, linear, sigmoid, and hyperbolic tangent functions are the most widely used activation functions.

To minimize the objective function ($F_o$), the weights of the network are adjusted in the calibration process of the back-propagation algorithm. In addition, the gradient descent method is employed to tune the weights along the negative direction of the gradient of $F_o$. The function $F_o$ is expressed as follows:

$$F_o = \frac{\sum_{j=1}^{q} \left(\hat{y}_j - y_j\right)^2}{2} \quad (2)$$

The weight adjustment process is repeated until convergence is achieved. The process of determining the weights has been detailed in previous studies (Haykin 1994, Hagan *et al.* 1996).

## 2.2 Adaptive neuro-fuzzy inference systems

An ANFIS is a network-based fuzzy inference system integrated with a learning algorithm that can learn autonomously from data. Jang (1993) was the first to develop an ANFIS, which comprises two main parts: (1) an adaptive network architecture and (2) a hybrid learning algorithm. Fuzzy if–then rules are usually expressed as follows:

$$\text{if } x \text{ is } H_i, \text{ then } f_i = a_i^T x + b_i \qquad i = 1, 2, \ldots, K \quad (3)$$

where the "if" and "then" parts are referred to as the antecedent and consequent, respectively; $x$ is the input vector of the antecedent part; $f_i$ is the output of the consequent part; $a_i$ and $b_i$ are the parameters of the consequent part; $K$ is the number of rules; and $H_i$ is the antecedent fuzzy membership function value of the $i$th rule. The membership function can be of different types, such as a Gaussian, bell, triangular, trapezoidal, or sigmoidal function. For instance, a Gaussian membership function can be expressed as follows:

$$H(x) = e^{\frac{-(x-c)^2}{2\sigma^2}} \quad (4)$$

where $\sigma$ and $c$ are the parameters of the antecedent part. ANFIS theory has been extensively discussed in previous studies (Marinos 1969, Mamdani 1974, Jang 1993).

## 2.3 Support vector machine

SVM, which is a kernel-based supervised learning algorithm, was initially developed for classification before being used for regression. Support vector regression (SVR), which was developed from SVM, is a popular ML technique used for solving nonlinear regression problems (Drucker et al. 1996, Vapnik et al. 1996). A nonlinear mapping function is used to map the input space of SVR into a high-dimensional feature space (Wu et al. 2008). In the present study, SVR was used instead of a BPNN in the proposed model, for two major reasons. First, when BPNNs are trained, only one objective is used to minimize the empirical risk (or total error) according to the empirical risk minimization induction principle. However, in SVR, the empirical risk and model complexity are minimized synchronously according to the structural risk minimization (SRM) induction principle, which results in SVR having a stronger generalization capability than does a BPNN (Yu et al. 2006, Al-Anazi and Gates 2010). Second, the model structure and weights of a BPNN are decided through a trial-and-error procedure and an iterative process, respectively (i.e. an error back-propagation algorithm). However, the architecture and weights of SVR are determined in terms of a quadratic optimization problem, which can be solved rapidly by using a standard programming algorithm (Lin et al. 2009, Tsai et al. 2015). Determining the model structure and weights of a BPNN is considerably more time-consuming than is determining those of SVR. Therefore, SVR is more appropriate than a BPNN for the development of the hybrid model proposed in this paper. Detailed descriptions of the SRM principle (Liong and Sivapragasam 2002, Yu et al. 2006) and the methodology of SVR (Vapnik 1995, Vapnik et al. 1996) can be found in the literature.

## 2.4 Integration of SVM and the MOGA

To obtain optimal combinations of multiple input features, the SVM-MOGA algorithm was adopted in this study. The process of this algorithm is illustrated in Fig. 1. First, input factors, including inundation depth, are simulated using a hydrodynamic numerical model. According to the parameter settings, chromosomes composed of input variables and their lag lengths are encoded to generate the population in each iteration step. The SVM algorithm is then executed in the processing procedure of the MOGA, which is widely used in solving multi-objective optimization problems. Subsequently, objective functions are calculated using the simulated and forecasted values. When the last iteration is reached, Pareto-optimal solutions, which represent different compromises among the designed objective functions, are generated. In this study, outputs of the numerical model are utilized as the reference, rather than the observations at field sites, to evaluate the forecasting performance of the ML models.

In general, a Pareto-optimal solution can be obtained through a single execution of the MOGA. When a decision maker must simultaneously consider multiple objectives and the desired solution must satisfy these objectives, the objectives form a Pareto-optimal solution front. For instance, two objective functions, namely objective 1 maximum and objective 2 minimum, are considered (Fig. 2). For these objectives, solutions A, B, and C, which are Pareto-optimal solutions, are explicitly superior to solutions D, E, and F, which are dominated solutions. Pareto-optimal solutions represent optimal trade-offs among multiple objectives.

A simple approach to obtaining Pareto-optimal solutions involves the use of the generalized Pareto-based, scale-independent fitness function (GPSIFF). The core concept of the GPSIFF involves determining Pareto-optimal solutions by considering the quantitative fitness values of dominated and nondominated solutions in the objective space (Ho et al. 2004, Hou et al. 2008). The aforementioned function not only retains the concepts of domination proposed by Deb (2001) but also quantitatively evaluates solutions. Therefore, the GPSIFF was used to assess candidate individuals and obtain Pareto-optimal solutions in this study. Let the fitness value of a solution $M$ be a score acquired from all participant solutions according to the following function:

$$\text{GPSIFF}(M) = p - q + c \quad (5)$$

where $p$ is the number of solutions that can be dominated by $M$; $q$ is the number of solutions that can dominate $M$ in the objective space; and $c$ is the number of all participant solutions, which are used to acquire a positive fitness value. A Pareto-optimal solution means that the solution possesses the highest score value.

## 3 Application

### 3.1 Background of the study area

Taiwan, where typhoons occur frequently, especially during the summer season and fall season (from August to October), is located in the northwestern Pacific Ocean. Yilan County,
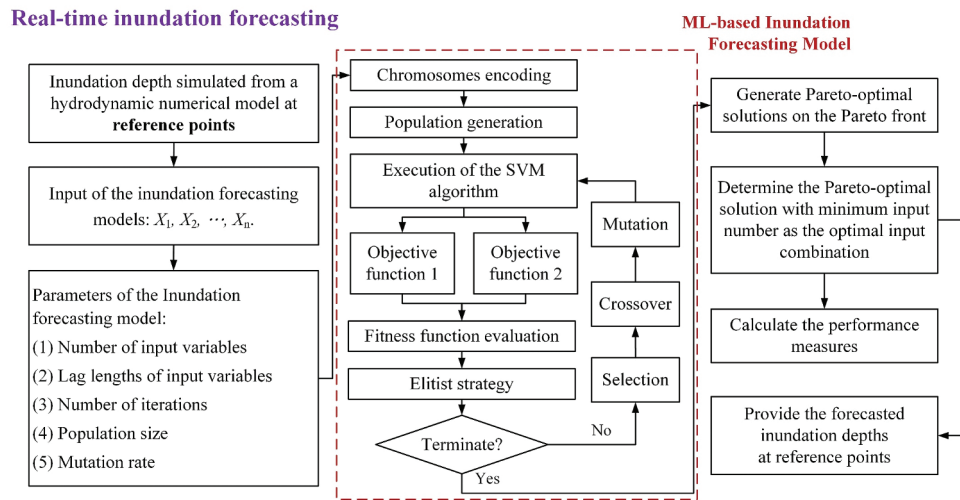
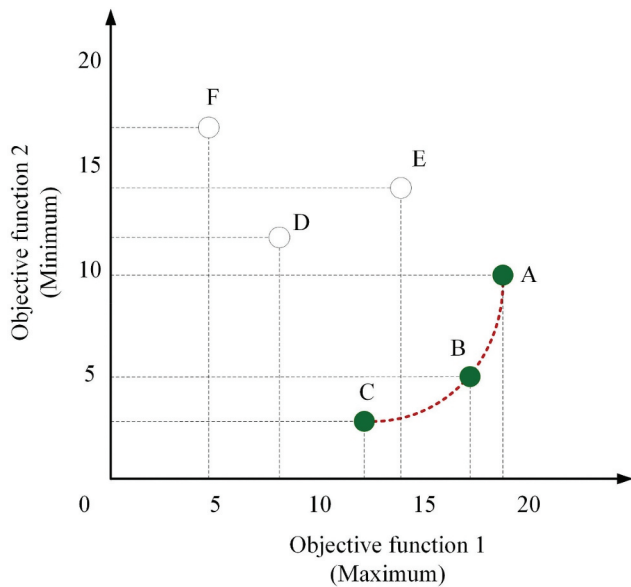**Figure 1.** Illustration of the SVM-MOGA-based algorithm.



**Figure 2.** Illustration of Pareto-optimal solutions (i.e., Solutions A, B, and C) on the Pareto front (i.e., the dotted line).

which is located in northeastern Taiwan (Fig. 3), was selected as the study area because of its long history of flooding problems. This county has an area of approximately 2143 km$^2$ and a population of more than 450 000 people, who mainly reside in low-altitude areas and experience considerable flooding-related problems. Yilan County has high altitudes in the west and low altitudes in the east. The northeast monsoon occurs in this county during autumn and winter. Nine inundation locations were used as reference points in this study. In summer, considerable convective rain occurs because of the increased temperature. The period from September to December is the typhoon season with the most rainfall. It rains more than 200 days a year in Yilan County, and the county's annual rainfall exceeds 2700 mm.

### 3.2 Data

#### 3.2.1 Rainfall data

Hourly rainfall data were collected from the Taiwan Water Resources Agency. The data of 16 rainfall gauges in Yilan County were used in this study (Fig. 3), and these gauges were grouped into three regions according to their spatial and terrain characteristics. Regions A, B, and C represent the upstream (i.e. mountainous area), downstream (i.e. flatland area), and other (i.e. located outside the Lanyang River basin) regions, respectively. Information on the considered raingauges is listed in Table 2. Table 3 lists the dates of occurrence and total duration of the historical typhoon events whose information was used as the training and testing data for predicting inundation depth in the next 1–6 h. Moreover, the rainfall estimated from integrated radar–raingauge data (KRID), obtained from radar reflectivity data with corrections made for raingauge observations with spatial and temporal resolutions of 0.0125° per hour, was used in this study to improve the prediction performance of the adopted models. The KRID is produced by the National Science and Technology Center for Disaster Reduction in Taiwan.

#### 3.2.2 Typhoon characteristics

To test the effects of typhoon characteristics on IF, data on these characteristics were collected from the typhoon land warnings issued by the Central Weather Bureau of Taiwan and used as model input. The typhoon characteristic data set employed in this study comprised data on seven factors: (1) the latitude and (2) the longitude of the typhoon centre (degree), (3) the distance between the typhoon centre and the inundation reference points (km), (4) the maximum wind speed near the centre of the typhoon (m/s), (5) the atmospheric pressure at the centre of the typhoon (hPa), (6) the storm radius of winds faster than 15 m/s (km), and (7) the speed of typhoon movement (km/h). The aforementioned factors are denoted as *X, Y, D, V, P, W*, and *S*, respectively, in this paper.
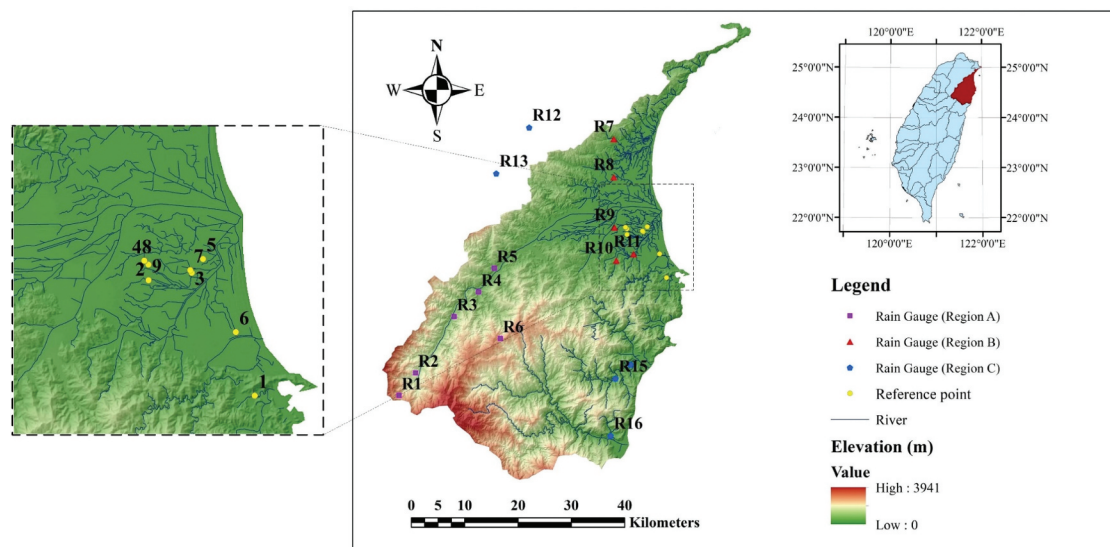
**Figure 3.** Location of Yilan County, inundation reference points, and raingauges in different regions.

### 3.2.3 Inundation simulation database

In this study, data preprocessing was conducted using an inundation database to obtain simulated inundation depths, as shown in Fig. 4. Boundary conditions must be determined when conducting the aforementioned simulation. A hydrodynamic numerical model should include at least three modules for the simulation of the rainfall–runoff procedure, channel and pipe, and overflow. A one-dimensional (1D) flow module can be used to calculate hydrographs of the overflow flow rate at sewer openings when the surface runoff exceeds the design capacity of a sewer system. The overflow hydrographs were subsequently used as sources of a 2D overland flow module.

The study area was divided into river areas, urban sewer areas, and surface runoff catchments. Simulations were conducted for each of these areas using different analysis modules. For river areas, the Soil Conservation Service curve number (CN) was used to analyse the runoff during different rainfall events on the basis of the land use. For urban sewer areas, a rational formula was used to calculate the surface runoff

**Table 2.** Main raingauge information.

| Serial number | Name | Longitude, E | Latitude, N | Elevation (m) | Region | Description |
|---|---|---|---|---|---|---|
| R1 | Si-Yuan | 121°20′55″ | 24°23′56″ | 2036.0 | A | Region A raingauges are located in the upstream region. |
| R2 | Nan-Shan | 121°22′46″ | 24°26′14″ | 1050.0 | A | |
| R3 | Liu-Mao-An | 121°27′4″ | 24°31′54″ | 585.0 | A | |
| R4 | Tu-Chang-1 | 121°29′47.5″ | 24°34′22.9″ | 400.0 | A | |
| R5 | Fan-Fan-2 | 121°31′32″ | 24°36′47″ | 295.0 | A | |
| R6 | Tai-Ping-Shan-1 | 121°32′11″ | 24°29′40″ | 1960.0 | A | |
| R7 | Wu-Feng | 121°44′22″ | 24°49′60″ | 83.0 | B | Region B raingauges are located in the downstream region. |
| R8 | Yi-Lan | 121°44′53″ | 24°45′56″ | 7.2 | B | |
| R9 | Xin-Bei-Cheng | 121°44′56″ | 24°40′51″ | 16.5 | B | |
| R10 | Xin-Liao-1 | 121°45′7″ | 24°37′30″ | 60.0 | B | |
| R11 | Dong-Shan | 121°47′2″ | 24°38′8″ | 5.0 | B | |
| R12 | Tong-Hou | 121°35′30″ | 24°51′00″ | 387.0 | C | Region C raingauges are located in the other region. |
| R13 | Xia-Pen | 121°31′49″ | 24°46′22″ | 589.0 | C | |
| R14 | Wu-Ta | 121°46′38.0″ | 24°26′58.0″ | 32.0 | C | |
| R15 | Zhang-Lin | 121°44′58″ | 24°25′33″ | 160.0 | C | |
| R16 | Da-Zhuo-Shui | 121°43′52.0″ | 24°19′51.0″ | 48.0 | C | |

**Table 3.** Description of the typhoon events used in this study with a land warning issued by Taiwan Central Weather Bureau (CWB).

| Number | Name | Date | Duration (h) |
|---|---|---|---|
| 1 | Sinlaku | 12 September 2008 | 87 |
| 2 | Parma | 4 October 2009 | 42 |
| 3 | Megi | 21 October 2010 | 54 |
| 4 | Saola | 31 July 2012 | 66 |
| 5 | Soudelor | 16 August 2015 | 60 |

discharge. A rainfall–runoff module with rainfall data was used to calculate surface runoff discharge hydrographs. Historical rainstorm event records are used for calibrating several parameters, such as the CN and Manning $n$ values.

Although multiple rainfall gauges were available in the study area, insufficient data were available regarding historical long-term inundation depths. Therefore, the physics-based numerical model SOBEK (Deltares; https://www.del
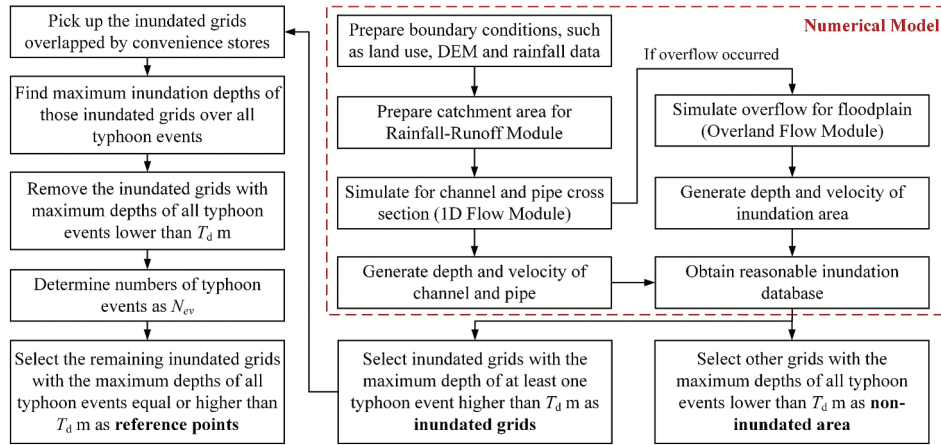
**Data preprocessing of inundation database**



Figure 4. Illustration of simulation of inundation depth by the SOBEK model.

tares.nl/en/; last accessed on 22 January 2021) was used to simulate the flow overflow process and inundation components of the study area. The SOBEK model was used to solve the St Venant equations (Delft Hydraulics 2013) and contained three major modules: a rainfall–runoff module, a 1D flow module, and a 2D overland flow module. The finite-difference scheme of SOBEK is commonly used for simulating unsteady flow velocities, water levels, and inundation extents associated with flooding events in rivers and urban sewer or drainage systems (Verwey *et al.* 2008, Kuntiyawichai *et al.* 2011, Prinsen and Becker 2011, Delft Hydraulics 2013, Doong *et al.* 2016, Yang *et al.* 2018). Technical details regarding the SOBEK model can be found in Delft Hydraulics (2013).

The inundation database generated using the aforementioned numerical model was separated into data for inundated and noninundated regions according to the depth threshold $T_d$ to remove negligible depth results. The data were separated using the following equation:

$$D = \begin{cases} d, d > T_d \, (m) \\ 0, \text{Otherwise} \end{cases} \quad (6)$$

where $D$ and $d$ represent the inundation depth factor and the factor value, respectively. In this study, the $T_d$ value was set as 0.3 m (Pan *et al.* 2012).

### 3.3 Model setting

#### 3.3.1 Model development
Figure 5 illustrates the flow of model development in this study, which comprises three steps: (1) comparing the accuracy of BPNN-, ANFIS-, SVM-, and SVM-MOGA-based models when using factors such as inundation depth and weighted average rainfall as model inputs; (2) examining the effects of using different inputs for SVM-MOGA-based models; and (3) investigating the optimal input combinations and input lag lengths for the SVM-MOGA-based model with the highest accuracy.

In general, inundation depth and raingauge observations are the main factors used for the establishment of ML-based IF models. Pan *et al.* (2011) divided their study area into five control sub-areas with five raingauges using the Thiessen polygon method. Chang *et al.* (2014a) calculated the weighted average rainfall over a catchment area using the Thiessen polygon method and applied the calculated weighted average rainfall as an input for IF models; this was also done by Jhong *et al.* (2016, 2017). Pan *et al.* (2014) stated that the average rainfall of upstream regions must be acquired from all raingauges because of the uneven spatial distribution of rainfall. Factors such as inundation depth and weighted average rainfall were used as input benchmarks for the BPNN, ANFIS, SVM, and SVM-MOGA models (denoted as BPNN-1, ANFIS-1, SVM-1, and SVM-MOGA-1, respectively) in this study. Inundation depth forecasts for 1–6 h into the future were desired in this study. The general form of an ML-based IF model is expressed as follows:

$$\hat{D}_{t+\Delta t} = f(D_t, \, D_{t-1}, \ldots, \, D_{t-(L_D-1)}, O_{m,t}, \, O_{m,t-1}, \ldots, \\ O_{m,t-(L_{O_m}-1)}, O^a_{m,t}, \, O^a_{m,t-1}, \ldots, \, O^a_{m,t-\left(L_{O^a_m}-1\right)}) \quad (7)$$

where $D_t$, $O_{m,t}$, and $O^a_{m,t}$ represent the inundation depth, mean value of raingauge observations, and accumulation of the mean value of raingauge observations at time $t$, respectively. The parameter $\Delta t$ is the lead time period (from 1 to 6 h); $\hat{D}_{t+\Delta t}$ represents the inundation depth forecasted for time $t + \Delta t$ by using an IF model; and $L_D$, $L_{O_m}$, and $L_{O^a_m}$ denote the lag lengths of $D$, $O_m$, and $O^a_m$, respectively. To determine the lagged variables for BPNN-1, ANFIS-1, and SVM-1, the linear transfer function (LTF) was adopted, where the least-squares technique was used to construct a linear function with lagged input variables. On the basis of the $t$ test results, the lagged variables of BPNN-1, ANFIS-1, and SVM-1 are the antecedent 1 and 4 h rainfall, antecedent 1, 2, 4, and 5 h accumulated rainfall, and antecedent 1 h inundation depth, which were used as model inputs. The related model code can be found in the Supplementary material.
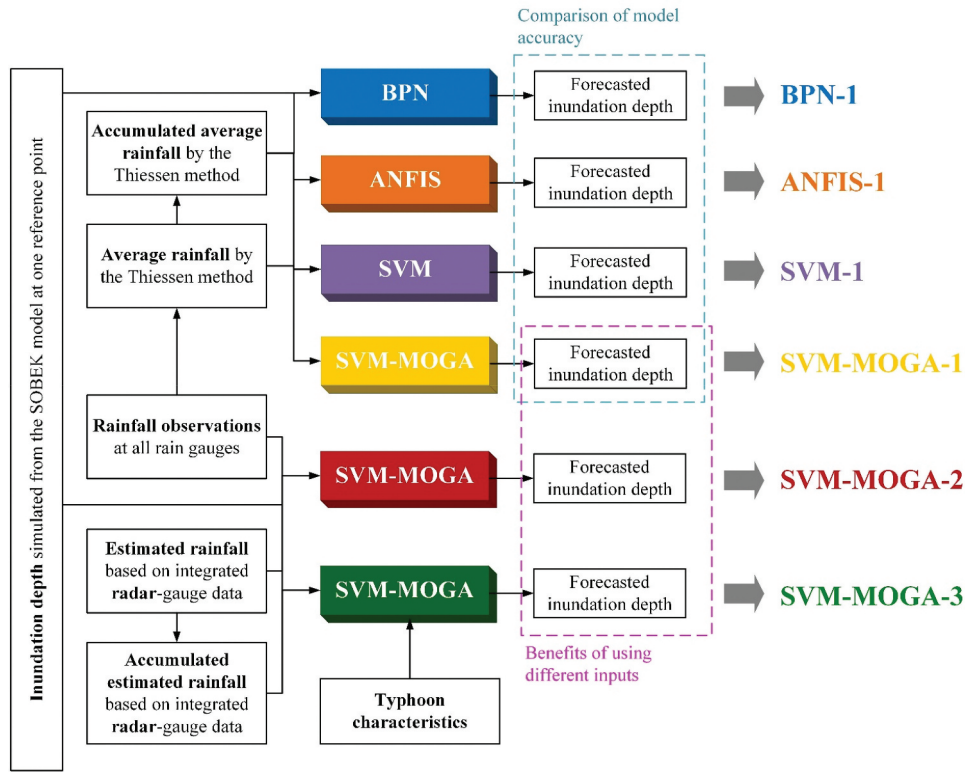
**Figure 5.** Flowchart of model development in this study.

The aforementioned factors are insufficient for IF because the weighted average rainfall of upstream regions obtained using the Thiessen polygon method cannot be used to determine spatial rainfall features. Another commonly used input factor for ML-based IF models is the total rainfall observation of multiple raingauges. Chang *et al.* (2010) used the current and past rainfall data of five nearby raingauges. Pan *et al.* (2011) used the rainfall observation and rainfall accumulation data of five nearby raingauges for the previous 22 h to develop a rainfall–inundation artificial neural network model. Shen and Chang (2013) employed historical and design rainfall events with different return periods for three nearby raingauges. Nevertheless, even though the total rainfall observation of multiple raingauges was generally used as model input in previous studies, the use of that is relatively lacking in spatial combinatorial optimization of multiple input features in upstream regions. Thus, the effective extraction of the spatial information of all raingauges in a study area is extremely advantageous for IF. Moreover, radar-based rainfall data are widely used in various applications, especially urban flood forecasting and IF (e.g. Chen *et al.* 2019, Yoon 2019, Lee *et al.* 2020).

To demonstrate the high accuracy of the developed hybrid method and to investigate the benefits of integrating raingauge observations and radar-based rainfall data, the inundation depth, radar-based rainfall data, and observations of all raingauges in the study area were used as inputs of SVM-MOGA-2. The general form of SVM-MOGA-2 is as follows:

$$\hat{D}_{t+\Delta t} = f_{\text{SVM} - \text{MOGA}}(D_t,\ D_{t-1}, \ldots,\ D_{t-(L_D-1)}, R_{r,t},\ R_{r,t-1}, \ldots,$$
$$R_{r,t-(L_{R_r}-1)}, R^a_{r,t},\ R^a_{r,t-1}, \ldots,\ R^a_{r,t-\left(L_{R^a_r}-1\right)},$$
$$\mathbf{O}_{t,t},\ \mathbf{O}_{t,t-1}, \ldots,\ \mathbf{O}_{t,t-\left(L_{\mathbf{O}_t}-1\right)})$$

$$(8)$$

where $R_{r,t}, R^a_{r,t}$, and $\mathbf{O}_{t,t}$ represent the rainfall obtained from radar data, the rainfall accumulation obtained from radar data, and the rainfall observations of all 16 raingauges in the study area at time $t$, respectively. The parameters $L_{R_r}$, $L_{R^a_r}$, and $L_{\mathbf{O}_t}$ denote the lag lengths of $R_r$, $R^a_r$, and $\mathbf{O}_t$, respectively. In addition, to investigate the influence of typhoon characteristics on IF, these characteristics and the inputs of SVM-MOGA-2 were used as inputs of SVM-MOGA-3. The general form of SVM-MOGA-3 is as follows:

$$\hat{D}_{t+\Delta t} = f_{\text{SVM} - \text{MOGA}}(D_t,\ D_{t-1}, \ldots,\ D_{t-(L_D-1)},$$
$$R_{r,t},\ R_{r,t-1}, \ldots,\ R_{r,t-(L_{R_r}-1)}, R^a_{r,t},\ R^a_{r,t-1}, \ldots,\ R^a_{r,t-\left(L_{R^a_r}-1\right)},$$
$$\mathbf{O}_{t,t},\ \mathbf{O}_{t,t-1}, \ldots,\ \mathbf{O}_{t,t-\left(L_{\mathbf{O}_t}-1\right)}, \mathbf{T}_t, \mathbf{T}_{t-1}, \ldots,\ \mathbf{T}_{t-(L_{\mathbf{T}}-1)})$$

$$(9)$$

where $\mathbf{T}_t$ represents seven typhoon characteristics at time $t$, and $L_{\mathbf{T}}$ denotes the lag lengths of $\mathbf{T}$.

### 3.3.2 Parameters

A crucial step in ML is the determination of appropriate model parameters. In this study, BPNN-1 comprised three layers: an input layer, a hidden layer, and an output layer. Five hidden nodes were used in the hidden layer of BPNN-1. The transfer function of the hidden layer was the LTF. Each input variable for ANFIS-1 had three

membership functions with Gaussian distributions. In addition, the numbers of input variables for SVM-MOGA-1, SVM-MOGA-2, and SVM-MOGA-3 were 3, 19, and 26, respectively. The number of iterations and population size were set as 5 and 50, respectively, for SVM-MOGA-1. Moreover, for SVM-MOGA-2 and SVM-MOGA-3, the number of iterations and population size were set as 50 and 500, respectively. Because a one-gene mutation operation with a mutation rate was adopted to produce new chromosomes, a probability was randomly generated for a selected chromosome. Therefore, the mutation rate for all the models was set as 0.05 in this study. A lower mutation rate represents a lower probability that mutation occurs. Furthermore, considering the size of the spatial domain and the relationship between the model input and the desired output, the lag lengths of input variables for all the models were set as 2; thus, the aforementioned SVM-MOGA-based models can optimize all input variables with lag lengths of $t$, $t - 1$, and $t - 2$.

### 3.3.3 Performance metrics

In this study, the root mean square error (RMSE) and mean absolute error (MAE), two criteria frequently used for evaluating the performance of ML-based forecasting models (Tabari *et al.* 2012), were adopted as model performance metrics. RMSE and MAE were used to measure the difference between the simulated and forecasted inundation depths. Lower RMSE and MAE values represent better model performance. In the MOGA, the fitness value of a chromosome is assessed on the basis of objective functions. RMSE and MAE were adopted as objective functions for training the SVM-MOGA-based models developed in this study. These metrics are expressed as follows:

$$\text{RMSE}(\varphi) = \frac{1}{N_{ev}} \sum_{i=1}^{N_{ev}} \left\{ \sqrt{\frac{1}{n} \sum_{t=1}^{n} \left[ D_t - \hat{D}_t(\varphi) \right]^2} \right\}_i \qquad (10)$$

$$\text{MAE}(\varphi) = \frac{1}{N_{ev}} \sum_{i=1}^{N_{ev}} \left[ \frac{1}{n} \sum_{t=1}^{n} \left| D_t - \hat{D}_t(\varphi) \right| \right]_i \qquad (11)$$

where $\varphi$ denotes the combination of model inputs obtained from an SVM-MOGA-based model; $N_{ev}$ is the number of typhoon events; $n$ is the number of forecasts; and $D_t$ and $\hat{D}_t(\varphi)$ represent the simulated and forecasted inundation depths at time $t$, respectively.

Two additional parameters were used to evaluate model accuracy: the coefficient of efficiency (CE) and coefficient of correlation (CC). CE is frequently used to evaluate the forecasting ability of hydrological models, and CC represents the linear dependence between two investigated variables. CE and CC are equal to 1 if the forecasts are perfectly accurate. These parameters are expressed as follows:

$$\text{CE}(\varphi) = \frac{1}{N_{ev}} \sum_{i=1}^{N_{ev}} \left\{ 1 - \frac{\sum_{t=1}^{n} \left[ D_t - \hat{D}_t(\varphi) \right]^2}{\sum_{t=1}^{n} \left( D_t - \bar{D} \right)^2} \right\}_i \qquad (12)$$

$$\text{CC}(\varphi) = \frac{1}{N_{ev}} \sum_{i=1}^{N_{ev}} \left\{ \frac{\sum_{t=1}^{n} (D_t - \bar{D}) \left[ \hat{D}_t(\varphi) - \overline{\hat{D}}(\varphi) \right]}{\sqrt{\sum_{t=1}^{n} (D_t - \bar{D})^2 \sum_{t=1}^{n} \left[ \hat{D}_t(\varphi) - \overline{\hat{D}}(\varphi) \right]^2}} \right\}_i \qquad (13)$$

where $\bar{D}$ is the average simulated inundation depth and $\overline{\hat{D}}(\varphi)$ is the average forecasted inundation depth.

### 3.4 Model validation

In general, a crucial step in the construction of ML-based forecasting models is the selection of the number of training and testing events. Different results might be generated, and various conclusions might be inferred when selecting different training and testing data sets. To avoid this problem, the cross-validation method was used to assess model performance in this study. In the cross-validation method, data for each typhoon event were alternately used as the testing set, and the data for the remaining events were regarded as training sets.

As displayed in Fig. 6, data for Typhoon Megi (2010) and Typhoon Saola (2012) were used to calibrate the simulations conducted using SOBEK, and data for Typhoon Parma (2009) were employed as validation data. After numerous simulations and adjustments, the final adjusted ranges of different parameters were as follows: (1) the CN value ranged from 57 to 98, (2) the Manning $n$ value for river and regional drainage ranged from 0.025 to 0.035, and (3) the Manning $n$ value for the rainwater channel ranged from 0.015 to 0.02. As displayed in Fig. 6, the survey area in the simulation (bounded by blue lines) was selected on the basis of field data. The calibration and validation results indicated that the SOBEK model reasonably simulated the inundation depth.

## 4 Results

### 4.1 Comparison of model accuracy in the training and testing phases

Tables 4–7 present the RMSE, MAE, CE, and CC values of the BPNN-1, ANFIS-1, SVM-1, and SVM-MOGA-1 models at all reference points in the training phase. The smaller the RMSE and MAE values, the higher the forecasting accuracy. The CE and CC values ranged from 0 to 1, with higher values representing more accurate forecasts. The results of this study clearly indicated that for 1–3-h (short)-lead-time forecasting, SVM-1 outperformed the other models in terms of RMSE, and SVM-MOGA-1 outperformed the other compared models in terms of MAE and CE. For 4–6-h (long)-lead-time forecasting, SVM-1 had higher accuracy than did the other compared models for all reference points. Among the models compared, SVM-1 exhibited the highest CC values for almost every lead time. BPNN-1 and ANFIS-1 exhibited poor prediction performance, irrespective of lead time.
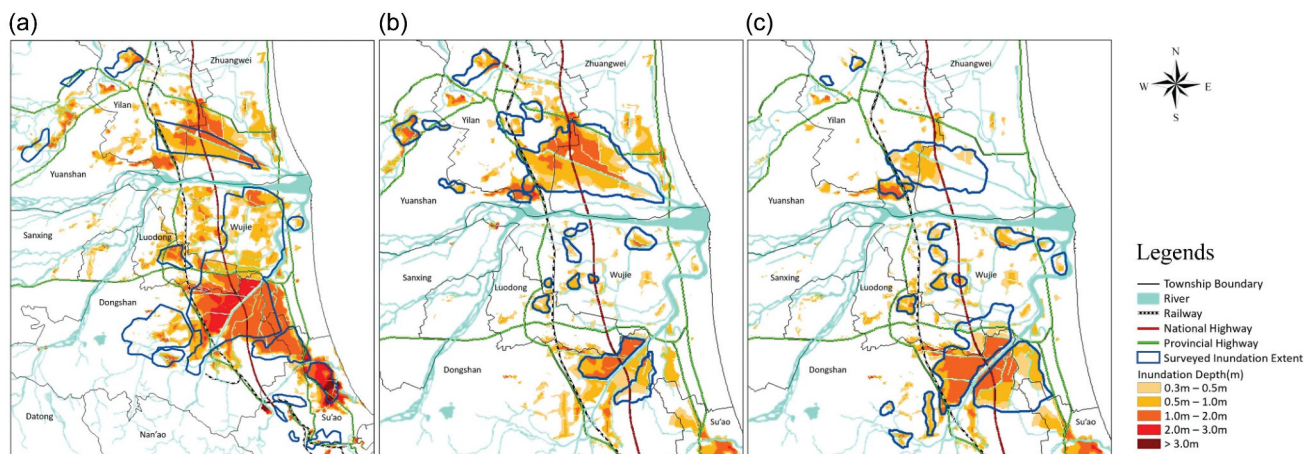
**Figure 6.** Inundation simulation results of SOBEK using (a) Typhoon Megi (2010) and (b) Typhoon Saola (2012) as calibration events and using (c) Typhoon Parma (2009) as a validation event.

Although SVM-1 exhibited the best performance among the compared models in the training phase, further testing was required. Figure 7 displays the RMSE, MAE, CE, and CC values obtained in the testing phase for the four ML-based IF models for all reference points. These values are displayed in terms of box plots. The RMSE and MAE values increased with lead time, whereas the CE and CC values decreased with lead time. As displayed in Fig. 7(a), SVM-MOGA-1 exhibited the lowest average RMSE and RMSE variance values among the compared models for lead times of 1–6 h. The average RMSE and RMSE variance values of the ANFIS-1 and SVM-1 models were higher than those of the other models. As depicted in Fig. 7(b), the trend of MAE values was similar to that of RMSE values. SVM-MOGA-1 exhibited the lowest MAE, and ANFIS-1 and SVM-1 exhibited relatively high MAE values. BPNN-

1 exhibited lower average MAE values than did the ANFIS-1 and SVM-1 models but higher average MAE values than did the SVM-MOGA-1 model. As shown in Fig. 7(c), SVM-MOGA-1 exhibited the highest average CE values and the lowest variance in CE values for all lead times. By contrast, SVM-1 exhibited the lowest average CE values and the highest variance in CE values for all lead times. For long-lead-time forecasting, BPNN-1 exhibited large variances in CE values. ANFIS-1 and SVM-1 exhibited negative CE values at most reference points, especially for lead times of 2–6 h. BPNN-1 exhibited negative CE values at some reference points for 4–6-h-lead-time forecasting. Thus, only SVM-MOGA-1 did not exhibit any negative CE values. As displayed in Fig. 7(d), ANFIS-1 and SVM-1 exhibited low average CC values and high variances in CC values. SVM-MOGA-1 exhibited the highest average CC

**Table 4.** RMSE values of BPN-1, ANFIS-1, SVM-1, and SVM-MOGA-1 at all reference points in the training phase.

| Lead time (h) | Model | Reference point | | | | | | | | |
|---|---|---|---|---|---|---|---|---|---|---|
| | | 1 | 2 | 3 | 4 | 5 | 6 | 7 | 8 | 9 |
| 1 | BPN-1 | 10.86 | 3.88 | 2.52 | 4.84 | 4.73 | 5.17 | 2.52 | 5.85 | 7.57 |
| | ANFIS-1 | 20.94 | 7.00 | 14.57 | 7.60 | 12.70 | 8.22 | 13.68 | 9.23 | 12.96 |
| | SVM-1 | **8.39** | 4.28 | 5.67 | 8.17 | 5.72 | 6.22 | 5.27 | 7.51 | **5.30** |
| | SVM-MOGA-1 | 10.05 | **2.58** | **1.52** | **3.98** | **2.74** | **3.96** | **1.51** | **4.93** | 6.52 |
| 2 | BPN-1 | 20.00 | 7.22 | 4.95 | 8.15 | 9.25 | 8.76 | 4.95 | 9.86 | 12.62 |
| | ANFIS-1 | 25.88 | 8.76 | 16.20 | 9.30 | 15.00 | 9.69 | 14.64 | 11.30 | 15.53 |
| | SVM-1 | **14.18** | **5.20** | 5.74 | 9.62 | **6.01** | 7.16 | 5.45 | 9.49 | **6.95** |
| | SVM-MOGA-1 | 16.36 | 5.40 | **3.47** | **6.83** | 6.32 | 7.55 | **3.51** | **8.38** | 11.28 |
| 3 | BPN-1 | 25.90 | 10.11 | 7.29 | 10.79 | 13.40 | 11.30 | 7.23 | 12.97 | 16.14 |
| | ANFIS-1 | 28.98 | 10.59 | 17.67 | 10.68 | 17.66 | 10.57 | 15.96 | 12.79 | 17.41 |
| | SVM-1 | **14.95** | **6.44** | 5.80 | 10.41 | **6.78** | **7.48** | 5.61 | **10.32** | **7.75** |
| | SVM-MOGA-1 | 20.28 | 8.36 | **5.25** | **8.93** | 9.93 | 9.80 | **5.25** | 10.96 | 14.74 |
| 4 | BPN-1 | 30.25 | 12.61 | 9.49 | 12.84 | 17.39 | 12.43 | 9.61 | 15.29 | 18.59 |
| | ANFIS-1 | 31.33 | 12.09 | 19.29 | 11.69 | 20.09 | 11.19 | 17.15 | 13.95 | 18.49 |
| | SVM-1 | **18.27** | **7.56** | **5.95** | **10.62** | **8.11** | **6.99** | **5.70** | **10.36** | **8.12** |
| | SVM-MOGA-1 | 23.41 | 10.54 | 7.18 | 10.65 | 14.08 | 11.12 | 7.09 | 12.88 | 16.67 |
| 5 | BPN-1 | 33.60 | 14.72 | 11.57 | 14.46 | 20.94 | 13.41 | 11.41 | 17.25 | 20.36 |
| | ANFIS-1 | 33.29 | 13.30 | 20.60 | 12.47 | 22.51 | 11.76 | 18.12 | 14.89 | 19.22 |
| | SVM-1 | **20.49** | **8.60** | **6.17** | **11.33** | **9.81** | **6.83** | **5.82** | **11.34** | **9.11** |
| | SVM-MOGA-1 | 25.99 | 12.50 | 8.78 | 12.19 | 17.91 | 11.95 | 8.46 | 14.34 | 17.83 |
| 6 | BPN-1 | 36.53 | 16.50 | 13.62 | 15.77 | 24.26 | 14.26 | 13.38 | 18.86 | 21.84 |
| | ANFIS-1 | 34.82 | 14.33 | 22.03 | 13.09 | 24.62 | 12.39 | 19.24 | 15.57 | 20.06 |
| | SVM-1 | **22.36** | **9.85** | **6.45** | **11.79** | **11.43** | **7.26** | **5.86** | **12.02** | **10.01** |
| | SVM-MOGA-1 | 28.42 | 14.29 | 10.11 | 13.27 | 21.15 | 12.61 | 9.82 | 15.56 | 18.69 |

**Table 5.** MAE values of BPN-1, ANFIS-1, SVM-1, and SVM-MOGA-1 at all reference points in the training phase.

| Lead time (h) | Model | Reference point | | | | | | | | |
|---|---|---|---|---|---|---|---|---|---|---|
| | | 1 | 2 | 3 | 4 | 5 | 6 | 7 | 8 | 9 |
| 1 | BPN-1 | 5.70 | 2.20 | 1.93 | 2.63 | 2.75 | 2.72 | 1.78 | 3.37 | 3.24 |
| | ANFIS-1 | 11.52 | 3.38 | 9.73 | 3.81 | 6.05 | 4.10 | 8.02 | 4.93 | 6.91 |
| | SVM-1 | 5.22 | 2.40 | 5.15 | 3.29 | 4.77 | 2.47 | 4.84 | 3.38 | 3.87 |
| | SVM-MOGA-1 | **3.32** | **1.04** | **1.12** | **1.56** | **1.32** | **1.68** | **1.06** | **1.96** | **2.05** |
| 2 | BPN-1 | 11.02 | 4.56 | 3.87 | 4.81 | 5.53 | 5.26 | 3.62 | 6.20 | 6.94 |
| | ANFIS-1 | 14.94 | 4.68 | 10.61 | 5.11 | 7.57 | 5.50 | 8.89 | 6.65 | 8.71 |
| | SVM-1 | 6.96 | 2.87 | 5.34 | 4.16 | 5.10 | **3.03** | 5.08 | 4.45 | 4.53 |
| | SVM-MOGA-1 | **5.99** | **2.13** | **2.14** | **2.90** | **2.45** | 3.22 | **2.09** | **3.66** | **3.96** |
| 3 | BPN-1 | 16.79 | 6.65 | 5.59 | 7.20 | 8.29 | 7.13 | 5.43 | 9.24 | 9.84 |
| | ANFIS-1 | 17.96 | 6.05 | 11.58 | 6.24 | 9.31 | 6.40 | 9.92 | 7.96 | 10.29 |
| | SVM-1 | **7.85** | 3.27 | 5.40 | 4.74 | 5.56 | **3.30** | 5.24 | **5.09** | **4.93** |
| | SVM-MOGA-1 | 8.36 | **3.26** | **3.19** | **3.97** | **4.15** | 4.42 | **2.89** | 5.24 | 5.69 |
| 4 | BPN-1 | 21.87 | 8.34 | 7.40 | 8.62 | 11.14 | 8.32 | 6.96 | 10.24 | 12.28 |
| | ANFIS-1 | 20.36 | 7.16 | 12.81 | 7.12 | 11.06 | 6.99 | 10.86 | 8.88 | 11.25 |
| | SVM-1 | **9.37** | **3.64** | 5.48 | **4.93** | 5.98 | **3.40** | 5.27 | **5.27** | **5.08** |
| | SVM-MOGA-1 | 10.30 | 4.38 | **4.44** | 4.98 | **5.73** | 5.31 | **4.24** | 6.41 | 7.00 |
| 5 | BPN-1 | 25.28 | 10.57 | 9.11 | 10.27 | 13.80 | 9.33 | 8.68 | 12.74 | 14.33 |
| | ANFIS-1 | 22.50 | 8.07 | 13.70 | 7.76 | 12.71 | 7.46 | 11.67 | 9.54 | 11.96 |
| | SVM-1 | **10.76** | **4.02** | **5.54** | **5.33** | **6.43** | **3.48** | 5.30 | **5.86** | **5.25** |
| | SVM-MOGA-1 | 12.12 | 5.47 | 5.84 | 5.99 | 7.37 | 6.00 | **5.14** | 7.40 | 7.89 |
| 6 | BPN-1 | 29.29 | 11.94 | 10.63 | 11.49 | 16.75 | 10.31 | 10.30 | 14.18 | 15.58 |
| | ANFIS-1 | 24.28 | 8.81 | 14.75 | 8.33 | 14.26 | 7.76 | 12.46 | 10.15 | 12.85 |
| | SVM-1 | **11.69** | **4.45** | **5.62** | **5.60** | **7.08** | **3.56** | **5.20** | **6.25** | **5.59** |
| | SVM-MOGA-1 | 13.63 | 6.49 | 6.85 | 6.70 | 9.00 | 6.68 | 6.27 | 8.19 | 8.63 |

**Table 6.** CE values of BPN-1, ANFIS-1, SVM-1, and SVM-MOGA-1 at all reference points in the training phase.

| Lead time (h) | Model | Reference point | | | | | | | | |
|---|---|---|---|---|---|---|---|---|---|---|
| | | 1 | 2 | 3 | 4 | 5 | 6 | 7 | 8 | 9 |
| 1 | BPN-1 | 0.949 | 0.977 | 0.998 | 0.936 | 0.993 | 0.910 | 0.997 | 0.934 | 0.952 |
| | ANFIS-1 | 0.775 | 0.912 | 0.924 | 0.763 | 0.948 | 0.668 | 0.917 | 0.768 | 0.821 |
| | SVM-1 | **0.967** | 0.966 | 0.988 | 0.622 | 0.989 | 0.809 | 0.987 | 0.834 | **0.973** |
| | SVM-MOGA-1 | 0.960 | **0.989** | **0.999** | **0.954** | **0.998** | **0.947** | **0.999** | **0.952** | 0.964 |
| 2 | BPN-1 | 0.809 | 0.914 | 0.992 | 0.789 | 0.974 | 0.678 | 0.990 | 0.785 | 0.852 |
| | ANFIS-1 | 0.626 | 0.849 | 0.906 | 0.592 | 0.924 | 0.478 | 0.899 | 0.601 | 0.727 |
| | SVM-1 | **0.905** | 0.949 | 0.987 | 0.399 | **0.988** | 0.735 | 0.985 | 0.707 | **0.951** |
| | SVM-MOGA-1 | 0.893 | **0.952** | **0.996** | **0.866** | **0.988** | **0.808** | **0.995** | **0.864** | 0.893 |
| 3 | BPN-1 | 0.631 | 0.824 | 0.981 | 0.517 | 0.945 | 0.284 | 0.978 | 0.546 | 0.724 |
| | ANFIS-1 | 0.480 | 0.759 | 0.881 | 0.371 | 0.898 | 0.283 | 0.880 | 0.413 | 0.625 |
| | SVM-1 | **0.890** | **0.920** | 0.987 | 0.213 | **0.984** | **0.705** | 0.984 | 0.617 | **0.939** |
| | SVM-MOGA-1 | 0.836 | 0.886 | **0.991** | **0.775** | 0.971 | 0.679 | **0.988** | **0.770** | 0.818 |
| 4 | BPN-1 | 0.427 | 0.687 | 0.967 | 0.297 | 0.905 | −0.096 | 0.961 | 0.328 | 0.608 |
| | ANFIS-1 | 0.339 | 0.645 | 0.862 | 0.117 | 0.857 | 0.087 | 0.861 | 0.214 | 0.546 |
| | SVM-1 | **0.833** | **0.885** | **0.986** | 0.123 | **0.977** | **0.746** | **0.984** | 0.579 | **0.933** |
| | SVM-MOGA-1 | 0.780 | 0.819 | 0.983 | **0.684** | 0.941 | 0.586 | 0.979 | **0.685** | 0.768 |
| 5 | BPN-1 | 0.177 | 0.515 | 0.949 | −0.221 | 0.855 | −0.468 | 0.939 | −0.285 | 0.492 |
| | ANFIS-1 | 0.194 | 0.528 | 0.829 | −0.142 | 0.818 | −0.133 | 0.834 | −0.004 | 0.495 |
| | SVM-1 | **0.778** | **0.845** | **0.985** | −0.019 | **0.967** | **0.755** | **0.983** | 0.474 | **0.915** |
| | SVM-MOGA-1 | 0.727 | 0.748 | 0.974 | **0.589** | 0.905 | 0.522 | 0.969 | **0.613** | 0.735 |
| 6 | BPN-1 | −0.262 | 0.275 | 0.925 | −0.853 | 0.802 | −1.296 | 0.913 | −1.266 | 0.389 |
| | ANFIS-1 | 0.049 | 0.391 | 0.802 | −0.420 | 0.782 | −0.397 | 0.809 | −0.216 | 0.427 |
| | SVM-1 | **0.727** | **0.789** | **0.983** | −0.052 | **0.954** | **0.710** | **0.983** | 0.412 | **0.896** |
| | SVM-MOGA-1 | 0.673 | 0.672 | 0.965 | **0.518** | 0.868 | 0.467 | 0.959 | **0.548** | 0.709 |

values. BPNN-1 exhibited similar CC values to SVM-MOGA-1 for short lead times and lower CC values than did SVM-MOGA-1 for long lead times.

The aforementioned results indicate that although SVM-1 exhibited the best performance in the training phase, SVM-MOGA-1 had higher accuracy than did SVM-1 in the testing phase; thus, overfitting problems might occur when using SVM-1, and the conventional approach of input determination is insufficient for IF. SVM-MOGA-1 is a more appropriate IF model than SVM-1 because the RMSE and MAE values of SVM-MOGA-1 are similar to those of SVM-1 but the CE values of SVM-1 at reference point 4 are negative for lead

times of 5–6 h. An SVM-MOGA-based algorithm is recommended for assessing input features for IF because such an algorithm has a higher capability of extracting useful input information than do conventional ML-based algorithms.

### 4.2 Benefits of using radar-based rainfall data for IF

To investigate the effects of using radar-based rainfall data and typhoon characteristics in model predictions, the forecasting performance of SVM-MOGA-1, SVM-MOGA-2, and SVM-MOGA-3 was compared (Tables 8–11 and Fig. 8). Tables 8–11 indicate the RMSE, MAE, CE, and CC values of the

**Table 7.** CC values of BPN-1, ANFIS-1, SVM-1, and SVM-MOGA-1 at all reference points in the training phase.

| Lead time (h) | Model | Reference point | | | | | | | | |
|---|---|---|---|---|---|---|---|---|---|---|
| | | 1 | 2 | 3 | 4 | 5 | 6 | 7 | 8 | 9 |
| 1 | BPN-1 | 0.976 | 0.989 | 0.999 | 0.969 | 0.997 | 0.957 | 0.999 | 0.969 | 0.977 |
| | ANFIS-1 | 0.913 | 0.966 | 0.965 | 0.976 | 0.976 | 0.896 | 0.962 | 0.930 | 0.936 |
| | SVM-1 | **0.987** | 0.990 | 0.996 | 0.930 | 0.997 | 0.950 | 0.996 | 0.959 | **0.992** |
| | SVM-MOGA-1 | 0.980 | **0.995** | **1.000** | **0.977** | **0.999** | **0.974** | **1.000** | **0.977** | 0.982 |
| 2 | BPN-1 | 0.915 | 0.960 | 0.996 | 0.909 | 0.987 | 0.870 | 0.995 | 0.909 | 0.934 |
| | ANFIS-1 | 0.860 | 0.945 | 0.957 | 0.893 | 0.968 | 0.843 | 0.957 | 0.889 | 0.903 |
| | SVM-1 | **0.959** | **0.983** | 0.996 | 0.906 | **0.997** | **0.927** | 0.996 | **0.933** | **0.985** |
| | SVM-MOGA-1 | 0.948 | 0.977 | **0.998** | **0.933** | 0.994 | 0.904 | **0.998** | 0.932 | 0.947 |
| 3 | BPN-1 | 0.854 | 0.920 | 0.991 | 0.836 | 0.974 | 0.772 | 0.989 | 0.840 | 0.888 |
| | ANFIS-1 | 0.820 | 0.915 | 0.949 | 0.854 | 0.954 | 0.804 | 0.947 | 0.854 | 0.876 |
| | SVM-1 | **0.954** | **0.972** | 0.996 | **0.891** | **0.996** | **0.917** | 0.996 | **0.922** | **0.980** |
| | SVM-MOGA-1 | 0.920 | 0.945 | 0.996 | 0.886 | 0.986 | 0.834 | 0.994 | 0.884 | 0.910 |
| 4 | BPN-1 | 0.794 | 0.871 | 0.984 | 0.756 | 0.956 | 0.703 | 0.981 | 0.764 | 0.847 |
| | ANFIS-1 | 0.786 | 0.888 | 0.936 | 0.822 | 0.942 | 0.773 | 0.936 | 0.822 | 0.858 |
| | SVM-1 | **0.930** | **0.959** | **0.995** | **0.886** | **0.993** | **0.927** | **0.995** | **0.924** | **0.976** |
| | SVM-MOGA-1 | 0.892 | 0.913 | 0.992 | 0.841 | 0.972 | 0.782 | 0.990 | 0.840 | 0.886 |
| 5 | BPN-1 | 0.739 | 0.816 | 0.975 | 0.675 | 0.935 | 0.633 | 0.971 | 0.687 | 0.812 |
| | ANFIS-1 | 0.753 | 0.859 | 0.928 | 0.792 | 0.926 | 0.740 | 0.930 | 0.793 | 0.842 |
| | SVM-1 | **0.912** | **0.945** | **0.994** | **0.863** | **0.989** | **0.930** | **0.995** | **0.905** | **0.968** |
| | SVM-MOGA-1 | 0.866 | 0.875 | 0.988 | 0.796 | 0.954 | 0.744 | 0.986 | 0.805 | 0.871 |
| 6 | BPN-1 | 0.681 | 0.759 | 0.965 | 0.592 | 0.912 | 0.559 | 0.959 | 0.610 | 0.780 |
| | ANFIS-1 | 0.724 | 0.831 | 0.915 | 0.765 | 0.910 | 0.695 | 0.918 | 0.770 | 0.823 |
| | SVM-1 | **0.894** | **0.924** | **0.993** | **0.834** | **0.984** | **0.918** | **0.994** | **0.885** | **0.961** |
| | SVM-MOGA-1 | 0.838 | 0.835 | 0.983 | 0.762 | 0.936 | 0.706 | 0.980 | 0.778 | 0.859 |

aforementioned models at all reference points in the training phase. The results indicate that SVM-MOGA-1 had the lowest accuracy among the three SVM-MOGA-based methods. SVM-MOGA-2 and SVM-MOGA-3 exhibited low MAE and RMSE values for 1–2-h-lead-time forecasting; however, only SVM-MOGA-3 exhibited low MAE and RMSE values for 3–6-h-lead-time forecasting. SVM-MOGA-2 and SVM-MOGA

-3 exhibited low CC and CE values for short-lead-time forecasting; however, only SVM-MOGA-3 exhibited low CC and CE values for long-lead-time forecasting.

Figure 8 depicts the values of the four performance metrics for SVM-MOGA-1, SVM-MOGA-2, and SVM-MOGA-3 for all the reference points in the testing phase. These values are displayed as box plots. As shown in Fig. 8(a), SVM-MOGA-3
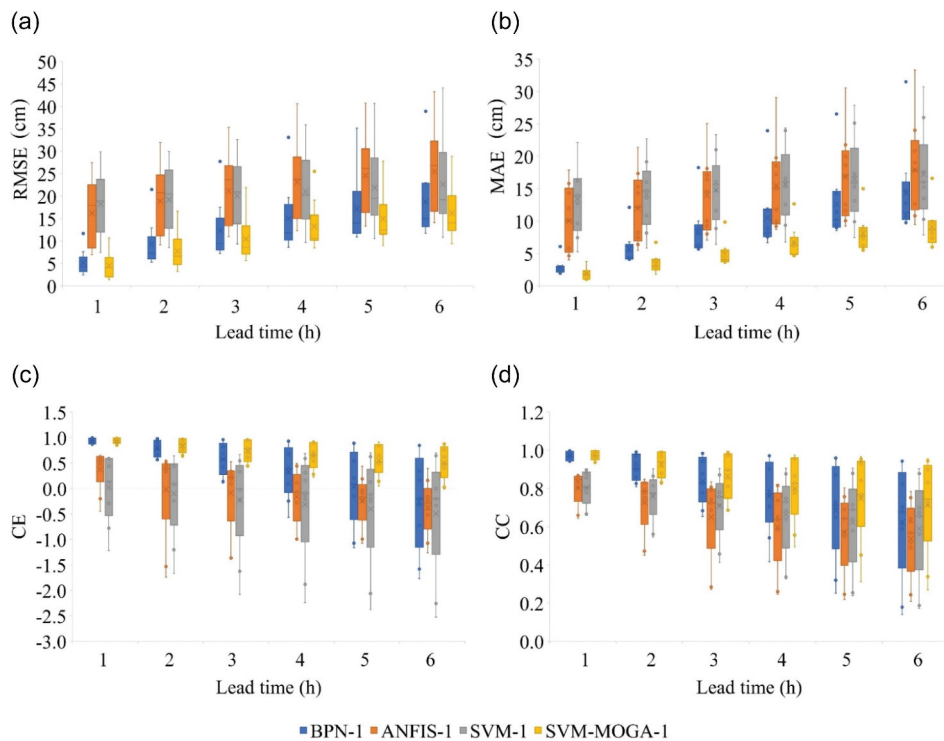


**Figure 7.** (a) RMSE, (b) MAE, (c) CE, and (d) CC values of BPN-1, ANFIS-1, SVM-1, and SVM-MOGA-1 in the testing phase.

**Table 8.** RMSE values of SVM-MOGA-1, SVM-MOGA-2, and SVM-MOGA-3 at all reference points in the training phase.

| Lead time (h) | Model | Reference point | | | | | | | | |
|---|---|---|---|---|---|---|---|---|---|---|
| | | 1 | 2 | 3 | 4 | 5 | 6 | 7 | 8 | 9 |
| 1 | SVM-MOGA-1 | 10.05 | 2.58 | 1.52 | 3.98 | 2.74 | 3.96 | 1.51 | 4.93 | 6.52 |
| | SVM-MOGA-2 | 8.61 | **1.25** | **1.25** | 3.05 | 2.36 | **2.45** | 1.11 | 4.00 | **4.97** |
| | SVM-MOGA-3 | **8.26** | 1.30 | 1.30 | **3.04** | **2.09** | 2.52 | **1.08** | **3.92** | 5.09 |
| 2 | SVM-MOGA-1 | 16.36 | 5.40 | 3.47 | 6.83 | 6.32 | 7.55 | 3.51 | 8.38 | 11.28 |
| | SVM-MOGA-2 | 13.15 | **3.01** | 2.00 | 5.32 | 4.61 | **5.10** | 1.58 | 6.80 | 8.69 |
| | SVM-MOGA-3 | **12.48** | 3.07 | **1.85** | **5.27** | **4.01** | 5.11 | **1.51** | **6.53** | **8.67** |
| 3 | SVM-MOGA-1 | 20.28 | 8.36 | 5.25 | 8.93 | 9.93 | 9.80 | 5.25 | 10.96 | 14.74 |
| | SVM-MOGA-2 | 15.67 | 4.75 | 2.77 | 7.25 | 6.47 | 7.09 | 2.25 | 9.02 | 11.68 |
| | SVM-MOGA-3 | **15.22** | **4.73** | **2.50** | **6.96** | **5.67** | **6.81** | **2.06** | **8.55** | **11.38** |
| 4 | SVM-MOGA-1 | 23.41 | 10.54 | 7.18 | 10.65 | 14.08 | 11.12 | 7.09 | 12.88 | 16.67 |
| | SVM-MOGA-2 | 16.60 | 6.60 | 3.62 | 8.68 | 8.10 | 8.28 | 3.12 | 10.65 | 13.44 |
| | SVM-MOGA-3 | **16.02** | **6.47** | **2.99** | **7.88** | **6.70** | **7.93** | **2.53** | **9.77** | **12.79** |
| 5 | SVM-MOGA-1 | 25.99 | 12.50 | 8.78 | 12.19 | 17.91 | 11.95 | 8.46 | 14.34 | 17.83 |
| | SVM-MOGA-2 | 16.72 | 8.31 | 4.81 | 9.13 | 9.22 | 9.03 | 4.16 | 10.95 | 14.06 |
| | SVM-MOGA-3 | **16.28** | **8.09** | **3.59** | **8.27** | **7.93** | **8.33** | **3.16** | **10.08** | **13.13** |
| 6 | SVM-MOGA-1 | 28.42 | 14.29 | 10.11 | 13.27 | 21.15 | 12.61 | 9.82 | 15.56 | 18.69 |
| | SVM-MOGA-2 | 16.39 | 9.21 | 6.08 | 8.86 | 10.36 | 8.58 | 5.42 | 10.30 | 13.73 |
| | SVM-MOGA-3 | **15.83** | **8.77** | **4.29** | **8.13** | **8.36** | **8.11** | **4.06** | **9.49** | **12.72** |

**Table 9.** MAE values of SVM-MOGA-1, SVM-MOGA-2, and SVM-MOGA-3 at all reference points in the training phase.

| Lead time (h) | Model | Reference point | | | | | | | | |
|---|---|---|---|---|---|---|---|---|---|---|
| | | 1 | 2 | 3 | 4 | 5 | 6 | 7 | 8 | 9 |
| 1 | SVM-MOGA-1 | 3.32 | 1.04 | 1.12 | 1.56 | 1.32 | 1.68 | 1.06 | 1.96 | 2.05 |
| | SVM-MOGA-2 | **3.10** | **0.67** | **0.97** | **1.18** | 1.25 | **1.17** | 0.80 | **1.59** | **1.63** |
| | SVM-MOGA-3 | 3.15 | 0.69 | 0.99 | 1.23 | **1.13** | 1.22 | **0.78** | 1.68 | 1.74 |
| 2 | SVM-MOGA-1 | 5.99 | 2.13 | 2.14 | 2.90 | 2.45 | 3.22 | 2.09 | 3.66 | 3.96 |
| | SVM-MOGA-2 | 5.27 | **1.40** | 1.40 | **2.23** | 2.10 | 2.39 | 1.11 | 2.97 | **3.22** |
| | SVM-MOGA-3 | **5.19** | 1.43 | **1.29** | 2.26 | **2.04** | **2.37** | **1.03** | **2.93** | 3.23 |
| 3 | SVM-MOGA-1 | 8.36 | 3.26 | 3.19 | 3.97 | 4.15 | 4.42 | 2.89 | 5.24 | 5.69 |
| | SVM-MOGA-2 | 6.95 | 2.20 | 1.86 | 3.21 | 2.97 | 3.43 | 1.53 | 4.19 | 4.68 |
| | SVM-MOGA-3 | **6.75** | **2.14** | **1.64** | **3.11** | **2.79** | **3.22** | **1.37** | **3.99** | **4.61** |
| 4 | SVM-MOGA-1 | 10.30 | 4.38 | 4.44 | 4.98 | 5.73 | 5.31 | 4.24 | 6.41 | 7.00 |
| | SVM-MOGA-2 | 8.00 | 3.05 | 2.49 | 4.00 | 3.61 | 4.24 | 2.10 | 5.08 | 5.76 |
| | SVM-MOGA-3 | **7.66** | **2.97** | **1.96** | **3.86** | **3.43** | **3.83** | **1.60** | **4.82** | **5.61** |
| 5 | SVM-MOGA-1 | 12.12 | 5.47 | 5.84 | 5.99 | 7.37 | 6.00 | 5.14 | 7.40 | 7.89 |
| | SVM-MOGA-2 | 8.63 | 3.91 | 3.17 | 4.39 | 4.31 | 4.71 | 2.61 | 5.43 | 6.29 |
| | SVM-MOGA-3 | **8.27** | **3.87** | **2.36** | **4.07** | **3.86** | **4.27** | **1.97** | **4.96** | **6.01** |
| 6 | SVM-MOGA-1 | 13.63 | 6.49 | 6.85 | 6.70 | 9.00 | 6.68 | 6.27 | 8.19 | 8.63 |
| | SVM-MOGA-2 | 9.21 | 4.38 | 3.94 | 4.39 | 5.06 | 4.86 | 3.26 | 5.25 | 6.54 |
| | SVM-MOGA-3 | **9.14** | **4.27** | **2.83** | **4.08** | **4.40** | **4.45** | **2.44** | **4.80** | **5.98** |

**Table 10.** CE values of SVM-MOGA-1, SVM-MOGA-2, and SVM-MOGA-3 at all reference points in the training phase.

| Lead time (h) | Model | Reference point | | | | | | | | |
|---|---|---|---|---|---|---|---|---|---|---|
| | | 1 | 2 | 3 | 4 | 5 | 6 | 7 | 8 | 9 |
| 1 | SVM-MOGA-1 | 0.960 | 0.989 | 0.999 | 0.954 | 0.998 | 0.947 | 0.999 | 0.952 | 0.964 |
| | SVM-MOGA-2 | 0.970 | **0.997** | **1.000** | **0.973** | 0.998 | 0.980 | **1.000** | 0.969 | **0.979** |
| | SVM-MOGA-3 | **0.973** | **0.997** | 0.999 | **0.973** | **0.999** | 0.979 | **1.000** | **0.970** | 0.978 |
| 2 | SVM-MOGA-1 | 0.893 | 0.952 | 0.996 | 0.866 | 0.988 | 0.808 | 0.995 | 0.864 | 0.893 |
| | SVM-MOGA-2 | 0.930 | **0.985** | **0.999** | 0.920 | 0.994 | **0.913** | **0.999** | 0.911 | 0.936 |
| | SVM-MOGA-3 | **0.938** | 0.984 | **0.999** | **0.921** | **0.995** | 0.912 | **0.999** | **0.917** | **0.937** |
| 3 | SVM-MOGA-1 | 0.836 | 0.886 | 0.991 | 0.775 | 0.971 | 0.679 | 0.988 | 0.770 | 0.818 |
| | SVM-MOGA-2 | 0.900 | **0.963** | 0.997 | 0.852 | 0.987 | 0.831 | **0.998** | 0.844 | 0.886 |
| | SVM-MOGA-3 | **0.907** | **0.963** | **0.998** | **0.864** | **0.990** | **0.844** | **0.998** | **0.860** | **0.892** |
| 4 | SVM-MOGA-1 | 0.780 | 0.819 | 0.983 | 0.684 | 0.941 | 0.586 | 0.979 | 0.685 | 0.768 |
| | SVM-MOGA-2 | 0.888 | 0.929 | 0.996 | 0.790 | 0.981 | 0.770 | 0.996 | 0.785 | 0.849 |
| | SVM-MOGA-3 | **0.896** | **0.932** | **0.997** | **0.827** | **0.987** | **0.789** | **0.997** | **0.819** | **0.863** |
| 5 | SVM-MOGA-1 | 0.727 | 0.748 | 0.974 | 0.589 | 0.905 | 0.522 | 0.969 | 0.613 | 0.735 |
| | SVM-MOGA-2 | 0.884 | 0.889 | 0.992 | 0.770 | 0.975 | 0.725 | 0.993 | 0.775 | 0.835 |
| | SVM-MOGA-3 | **0.891** | **0.895** | **0.996** | **0.811** | **0.982** | **0.767** | **0.996** | **0.809** | **0.856** |
| 6 | SVM-MOGA-1 | 0.673 | 0.672 | 0.965 | 0.518 | 0.868 | 0.467 | 0.959 | 0.548 | 0.709 |
| | SVM-MOGA-2 | 0.888 | 0.864 | 0.987 | 0.786 | 0.969 | 0.969 | 0.987 | 0.803 | 0.843 |
| | SVM-MOGA-3 | **0.896** | **0.877** | **0.994** | **0.819** | **0.980** | **0.779** | **0.993** | **0.832** | **0.865** |

**Table 11.** CC values of SVM-MOGA-1, SVM-MOGA-2, and SVM-MOGA-3 at all reference points in the training phase.

| Lead time (h) | Model | Reference point | | | | | | | | |
|---|---|---|---|---|---|---|---|---|---|---|
| | | 1 | 2 | 3 | 4 | 5 | 6 | 7 | 8 | 9 |
| 1 | SVM-MOGA-1 | 0.980 | 0.995 | **1.000** | 0.977 | **0.999** | 0.974 | **1.000** | 0.977 | 0.982 |
| | SVM-MOGA-2 | 0.985 | **0.999** | **1.000** | 0.987 | **0.999** | 0.991 | **1.000** | 0.984 | **0.990** |
| | SVM-MOGA-3 | **0.987** | **0.999** | **1.000** | 0.987 | **0.999** | 0.990 | **1.000** | **0.985** | 0.989 |
| 2 | SVM-MOGA-1 | 0.948 | 0.977 | 0.998 | 0.933 | 0.994 | 0.904 | 0.998 | 0.932 | 0.947 |
| | SVM-MOGA-2 | 0.966 | **0.993** | **0.999** | 0.959 | 0.997 | 0.958 | **1.000** | 0.955 | 0.968 |
| | SVM-MOGA-3 | **0.970** | **0.993** | **0.999** | **0.960** | **0.998** | **0.959** | **1.000** | **0.959** | **0.969** |
| 3 | SVM-MOGA-1 | 0.920 | 0.945 | 0.996 | 0.886 | 0.986 | 0.834 | 0.994 | 0.884 | 0.910 |
| | SVM-MOGA-2 | 0.951 | **0.982** | **0.999** | 0.925 | 0.994 | 0.918 | **0.999** | 0.922 | 0.943 |
| | SVM-MOGA-3 | **0.955** | **0.982** | **0.999** | **0.932** | **0.995** | **0.929** | **0.999** | **0.930** | **0.946** |
| 4 | SVM-MOGA-1 | 0.892 | 0.913 | 0.992 | 0.841 | 0.972 | 0.782 | 0.990 | 0.840 | 0.886 |
| | SVM-MOGA-2 | 0.945 | 0.965 | 0.998 | 0.894 | 0.991 | 0.888 | 0.998 | 0.891 | 0.926 |
| | SVM-MOGA-3 | **0.950** | **0.967** | **0.999** | **0.915** | **0.994** | **0.899** | **0.999** | **0.911** | **0.933** |
| 5 | SVM-MOGA-1 | 0.866 | 0.875 | 0.988 | 0.796 | 0.954 | 0.744 | 0.986 | 0.805 | 0.871 |
| | SVM-MOGA-2 | 0.943 | 0.945 | 0.996 | 0.883 | 0.988 | 0.866 | 0.996 | 0.885 | 0.920 |
| | SVM-MOGA-3 | **0.947** | **0.948** | **0.998** | **0.908** | **0.991** | **0.890** | **0.998** | **0.906** | **0.930** |
| 6 | SVM-MOGA-1 | 0.838 | 0.835 | 0.983 | 0.762 | 0.936 | 0.706 | 0.980 | 0.778 | 0.859 |
| | SVM-MOGA-2 | 0.944 | 0.933 | 0.994 | 0.893 | 0.985 | 0.882 | 0.994 | 0.901 | 0.924 |
| | SVM-MOGA-3 | **0.950** | **0.941** | **0.997** | **0.914** | **0.990** | **0.898** | **0.997** | **0.920** | **0.935** |

did not have an explicit improvement in RMSE. The average RMSE values obtained for SVM-MOGA-2 and SVM-MOGA-1 were similar for lead times of 1–2 h; however, the average RMSE values of SVM-MOGA-2 were lower than those of SVM-MOGA-3 and SVM-MOGA-1 for lead times of 3–6 h. As depicted in Fig. 8(b), SVM-MOGA-1 and SVM-MOGA-2 exhibited low MAE values for short-lead-time and long-lead-time forecasting, respectively. SVM-MOGA-3 exhibited the highest average MAE values and highest variance in MAE values. As displayed in Fig. 8(c), SVM-MOGA-3 exhibited the lowest average CE values. Furthermore, SVM-MOGA-1 and SVM-MOGA-3 exhibited large variances in CE values. SVM-MOGA-2 exhibited the highest average CE values for a lead time of 3–6 h. The trend observed for the CC values was similar to that observed for the CE values (Fig. 8(d)).

According to the aforementioned results, SVM-MOGA-2 outperformed SVM-MOGA-1 and SVM-MOGA-3. This result indicates that the average rainfall obtained using the Thiessen polygon method is an unsuitable input parameter for IF models because it lacks spatial information. Therefore, the variances in the CE and CC values of SVM-MOGA-1 were large in the testing phase. The results also indicate that the use of rainfall observations of all raingauges in the watershed and radar-based rainfall data (which include spatial information) as input enhances the accuracy of an SVM-MOGA-based model. However, the addition of typhoon characteristics does not improve the forecasting performance of an SVM-MOGA-based model. Information on these characteristics might act as noise in the model.



**Figure 8.** (a) RMSE, (b) MAE, (c) CE, and (d) CC values of SVM-MOGA-1, SVM-MOGA-2, and SVM-MOGA-3 in the testing phase.
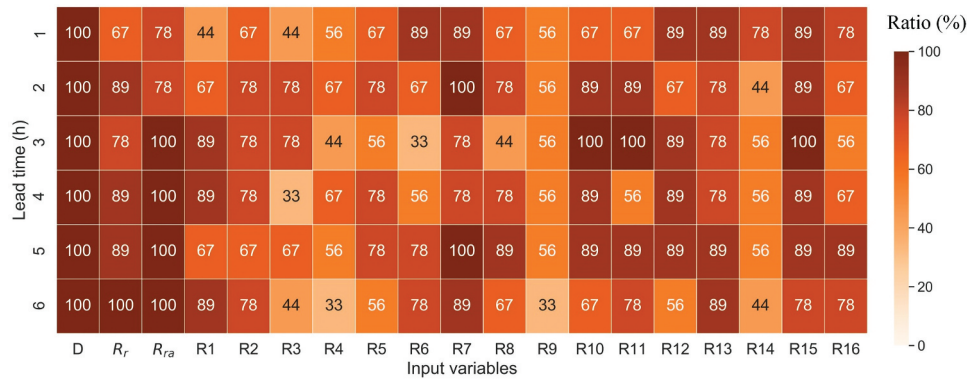
**Figure 9.** Percentage of reference points where the input variables are adopted by SVM-MOGA-2 for 1- to 6-h-ahead lead times.

### 4.3 Identification of effective input variables

On the basis of the aforementioned results, we attempted to identify effective input factors used by SVM-MOGA-2 in predictions for different lead times. Figure 9 shows the percentage of reference points adopted by SVM-MOGA-2 for all lead times. Because of the existence of different conditions of inundation depth, one forecasting model was constructed for one reference point in this study. A calculated number in one grid represents the number of reference points at which the forecasting model adopts an input variable at a certain lead time. As shown in Fig. 9, the usage percentages of inundation depth, radar-based rainfall observation data, and radar-based rainfall accumulation data near the reference points as inputs in the constructed models ranged from 78% to 100%, which indicates that these factors have high effectiveness in IF, particularly for long lead times. The results indicate that the data of most of the raingauges in Region A, especially those in R1 and R2, were important for IF because the usage percentages of these data as inputs in constructed models ranged from 67% to 89%. The use percentages of the data of the raingauges in Regions B and C by the constructed models ranged from 67% to 100%. Thus, these data were important input information for the constructed models.

### 4.4 Investigation of appropriate input lag lengths

To determine the variability of the lag lengths of each input variable for lead times of 1–6 h, we calculated the percentages of reference points for which the lag lengths of inundation

depth, radar-based rainfall observations, and radar-based rainfall accumulation data were adopted by SVM-MOGA-2 (Fig. 10). The inundation depth for a lag length of 0 is a crucial variable because it conveys the information that the aforementioned percentage increases with increasing lead times (Fig. 10(a)). In Fig. 10(b,c), the percentages near the lower right corner range from 78% to 100%, and the percentages near the upper left corner range from 33% to 67%. The results clearly indicate that the current inundation depth, radar-based rainfall observations, radar-based rainfall accumulation data, and factors with lag lengths of −1 and −2 are highly important inputs, especially for 4–6-h-lead-time forecasting. The inputs of inundation depth and radar-based rainfall are the variables at or near the reference points.

Figures 11–13 display the percentages of reference points for which the lag lengths of rainfall variables at various raingauges in Regions A (the upstream region), B (the downstream region), and C (the other region) were used by SVM-MOGA-2 for 1–6-h-lead-time forecasting, respectively. The results indicate that the current rainfall factors were beneficial for IF in Region A. Nevertheless, the use percentages of reference points for lag lengths of −1 and −2 were approximately 60% in this region, and the use percentages of reference points decreased with increasing lag lengths. Factors related to historical rainfall data in Region A were not important for IF in this region.

In Region B, most of the variables with lag lengths of 0 and −1 had high use percentages and thus were important for IF. The use percentages of the aforementioned variables ranged
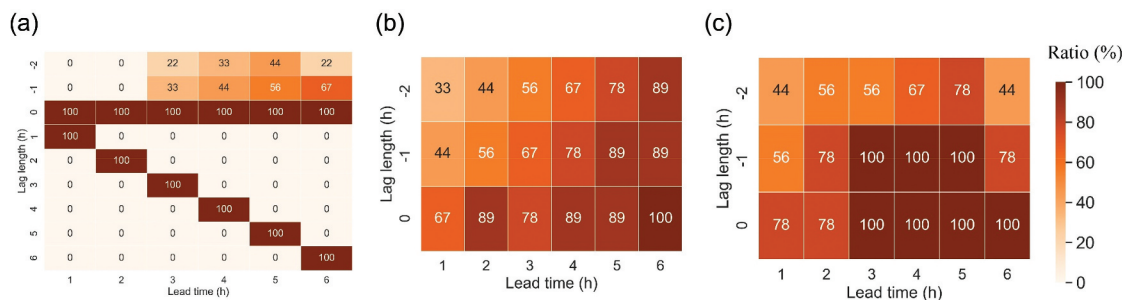


**Figure 10.** Percentages of reference points that the lag lengths of (a) inundation depth, (b) radar rainfall, and (c) accumulated radar rainfall are adopted by SVM-MOGA-2 for 1- to 6-h-ahead forecasts. A lag length of 0 means that the variables at time $t$ are used as input; a lag length of 1 means that the variables at time $t$ and $t − 1$ are used as input; a lag length of 2 means that the variables at time $t$, $t − 1$ and $t − 2$ are used as input.
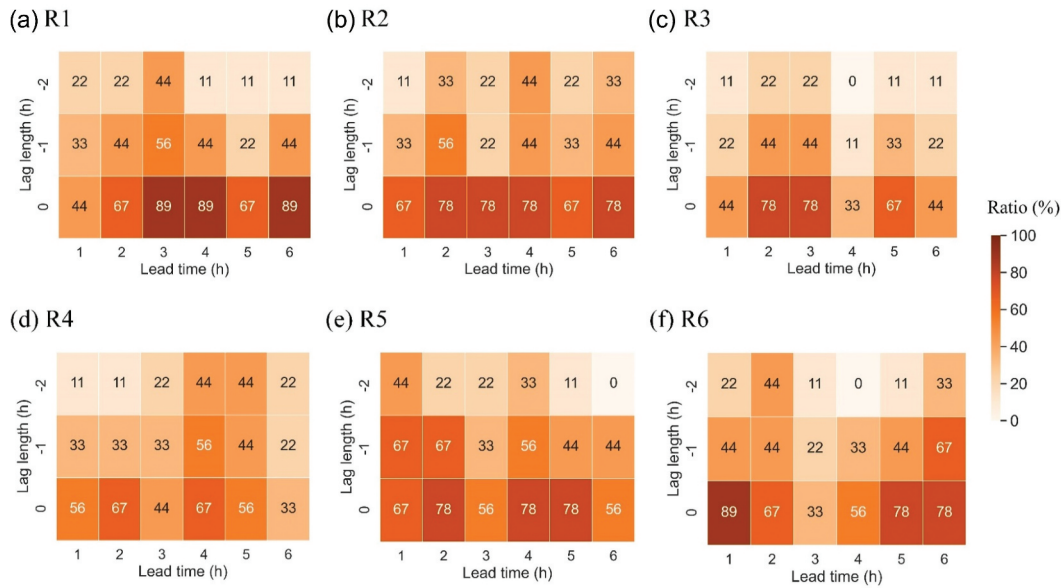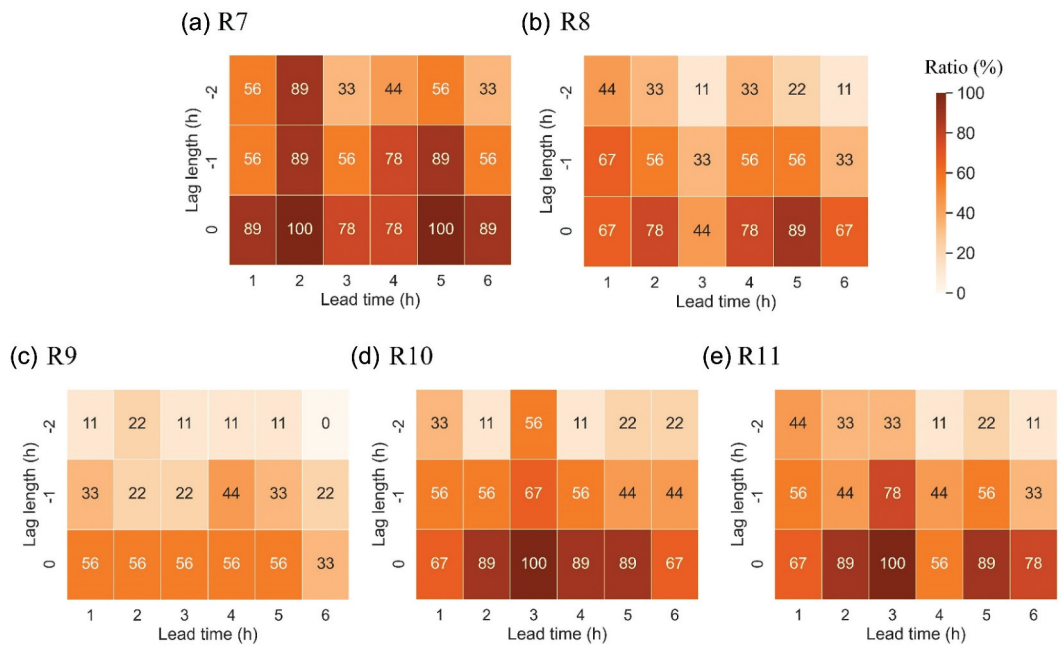
**Figure 11.** Percentages of reference points where the lag lengths of rainfall variables at different raingauges in Region A are adopted by SVM-MOGA-2 for 1- to 6-h-ahead forecasts.

A lag length of 0 means that the variables at time *t* are used as input; a lag length of 1 means that the variables at time *t* and *t* − *1* are used as input; a lag length of 2 means that the variables at time *t, t* − *1* and *t* − *2* are used as input.



**Figure 12.** Percentages of reference points where the lag lengths of rainfall variables at different raingauges in Region B are adopted by SVM-MOGA-2 for 1- to 6-h-ahead forecasts.

A lag length of 0 means that the variables at time t are used as input; a lag length of 1 means that the variables at time *t* and *t* − *1* are used as input; a lag length of 2 means that the variables at time *t, t* − *1* and *t* − *2* are used as input.

from 67% to 100% and from 56% to 89%, respectively. For R7 and R9, the rainfall variables with a lag length of −2 had a use percentage of less than 56%. Similar results were noted for Region C. For R14, the use percentages of the rainfall variables with lag lengths of 0 and −1 ranged from 67% to 100% and from 44% to 89%, respectively; thus, these variables had high importance for IF in Region C. The use percentages decreased with lag length. Overall, the results indicate that rainfall observations from the downstream and other regions are crucial data for improving the accuracy of IF.

## 5 Discussion

### 5.1 Influence of the addition of typhoon characteristics on an SVM-MOGA-based model

The results presented in Tables 8–11 and Fig. 8 indicate that the addition of typhoon characteristics to the SVM-MOGA-based model resulted in a decrease in its accuracy in the testing phase. This result contrasted with that obtained in the training phase. Thus, overfitting, which is a serious problem in neural network training, might occur
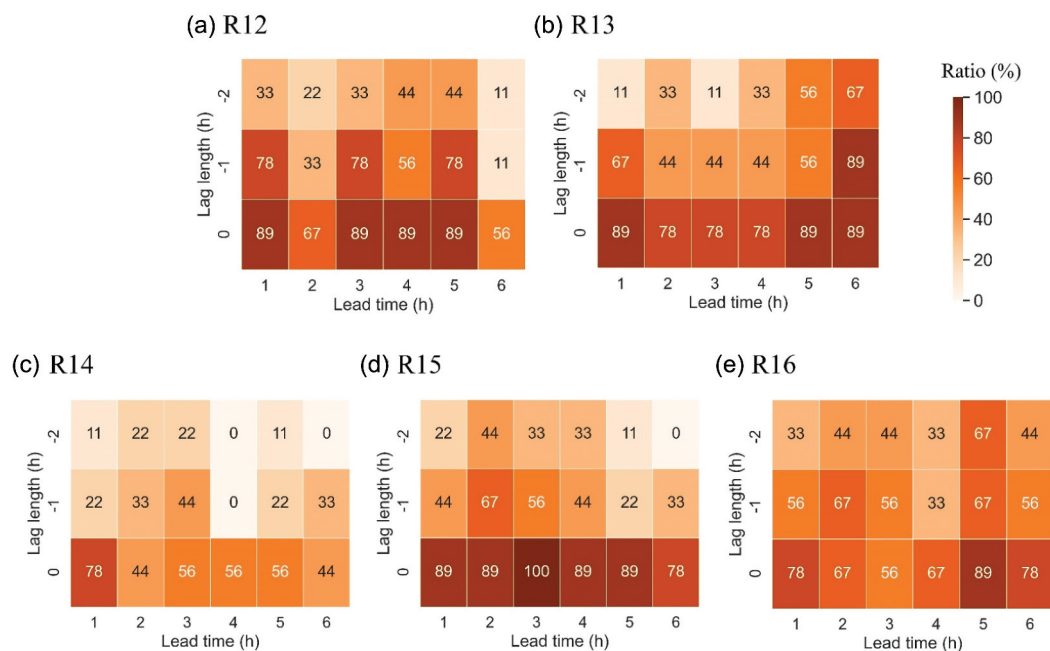
**Figure 13.** Percentages of reference points where the lag lengths of rainfall variables at different raingauges in Region C are adopted by SVM-MOGA-2 for 1- to 6-h-ahead forecasts.
A lag length of 0 means that the variables at time t are used as input; a lag length of 1 means that the variables at time t and t − 1 are used as input; a lag length of 2 means that the variables at time t, t − 1 and t − 2 are used as input.

in the training processes of an SVM-MOGA-based model. Several inferences can be made from the aforementioned result. First, because of the absence of rainfall observations over the ocean, detailed structures of the considered typhoons could not be obtained, as explained by Hsiao *et al.* (2015). Second, the current understanding of typhoons in the literature might be incomplete because errors and uncertainties are inevitable in typhoon intensity forecasting (DeMaria *et al.* 2014, Teng *et al.* 2020). Third, the influences of complex terrain and the Central Mountain Range (CMR) in Taiwan, which comprises steep mountains with an elevation of more than 3000 m, on rainfall are major reasons for uncertainties in typhoon intensity estimation.

Moreover, radar-based rainfall data and raingauge observations provide beneficial spatial information for IF; thus, an SVM-MOGA-based model that uses the aforementioned factors as inputs outperforms an SVM-MOGA-based model that uses typhoon characteristics in addition to these factors as inputs. Moreover, an SVM-MOGA-based model that uses radar-based rainfall and raingauge observations outperforms an SVM-MOGA-based model that uses only the weighted average rainfall as an input. According to the results of this study, radar-based rainfall data and raingauge observations are critical inputs for IF models, whereas typhoon characteristics are not. However, the finding related to typhoon characteristics is inconsistent with the conclusion of Jhong *et al.* (2016). One reason for this discrepancy is that Jhong *et al.* (2016) did not use radar-based rainfall data and raingauge observations for the upstream region in their predictions; thus, the addition of typhoon characteristics enhanced model accuracy in their study.

## 5.2 Spatial information on the optimized input features

In this study, combinatorial optimization was conducted for multiple input features to analyse the spatial information of rainfall variables important for IF. As displayed in Figs 10–13, the current and historical rainfall observations at most of the raingauges in the downstream region were more important for IF than were those in the upstream region. A reason for this result is that a majority of the watersheds in Taiwan exhibit complicated hydrological responses because of the complex terrain of the CMR (Hsiao *et al.* 2013); therefore, the rainfall in mountainous areas in Taiwan varies quickly within a few hours, particularly during typhoon landfall. Another reason for the aforementioned result is that relatively low correlation exists between the inundation depth at the downstream reference points and the rainfall observations at the upstream gauges. Therefore, historical rainfall observations at the upstream gauges are insufficient for accurate IF. By contrast, radar-based rainfall data and observations at downstream gauges are key features for the downstream inundation reference points because heavy rainfall in the downstream region may directly affect and cause flooding and inundation within a few hours.

In addition, the raingauge observations in the other region can provide useful information for IF even though the gauges are not located in the same watershed. A reason for this result is that the spatial scale of typhoons is larger than that of the study area. The storm radii of winds faster than 15 m/s in the typhoon events considered in this study were 200–300 km. However, the total area of Yilan County, Taiwan, is only approximately 2143 km$^2$, which is considerably smaller than the area covered by a typhoon. Thus, the rainfall at gauges in the other region is directly affected by the occurrence of typhoons in the study area. Therefore, the rainfall occurring in the other region can be adopted as valuable information for

IF. Overall, when using radar-based rainfall data and raingauge observations as inputs of the proposed SVM-MOGA-based model, the model can extract critical variables and determine an appropriate lag length for each input to analyse the spatial information of raingauge observations in various regions.

## 6  Conclusions

The accurate forecasting of hourly inundation depths during typhoons for disaster mitigation is challenging. To highlight the accuracy of ML-based IF models, we compared the accuracy of BPNN-, ANFIS-, SVM-, and SVM-MOGA-based models with consistent inputs. Radar-based rainfall data and raingauge observations were used as additional model inputs to extract optimal combinations of multiple input features. The developed hybrid SVM-MOGA-based model enabled (1) the analysis of critical input variables, (2) the investigation of appropriate lag lengths for each input variable, and (3) the evaluation of the spatial information of the rainfall variables in various regions adopted for IF during typhoon periods.

The training and testing results obtained for Yilan County, Taiwan, indicated that the developed hybrid model outperformed the other compared model when radar-based rainfall data and raingauge observations were used as inputs of the developed model. Results regarding the lag length of each input at each lead time indicate that the hybrid model can automatically select appropriate lag lengths of input variables and appropriate spatial information of optimized input features. Future studies can conduct systematic long-term observations of inundation depth rather than conduct simulations with numerical hydrodynamic models. Moreover, studies can increase the quality of the collected data by, for example, acquiring more accurate hourly typhoon characteristic data. In conclusion, the developed SVM-MOGA-based hybrid IF model is expected to be an efficient tool for early disaster warning systems.

## ORCID

Bing-Chen Jhong 🆔 http://orcid.org/0000-0003-3817-3946

## References

Al-Anazi, A. and Gates, I.D., 2010. A support vector machine algorithm to classify lithofacies and model permeability in heterogeneous reservoirs. *Engineering Geology*, 114 (3–4), 267–277. doi:10.1016/j.enggeo.2010.05.005

Bhola, P.K., Leandro, J., and Disse, M., 2018. Framework for offline flood inundation forecasts for two-dimensional hydrodynamic models. *Geosciences*, 8 (9), 346. doi:10.3390/geosciences8090346

Chang, L.C., et al., 2010. Clustering-based hybrid inundation model for forecasting flood inundation depths. *Journal of Hydrology*, 385 (1–4), 257–268. doi:10.1016/j.jhydrol.2010.02.028

Chang, F.J., et al., 2014a. Real-time multi-step-ahead water level forecasting by recurrent neural networks for urban flood control. *Journal of Hydrology*, 517, 836–846. doi:10.1016/j.jhydrol.2014.06.013

Chang, L.C., Shen, H.Y., and Chang, F.J., 2014b. Regional flood inundation nowcast using hybrid SOM and dynamic neural networks. *Journal of Hydrology*, 519, 476–489. doi:10.1016/j.jhydrol.2014.07.036

Chen, C.W., et al., 2019. Assessing landslide characteristics in a changing climate in northern Taiwan. *Catena*, 175, 263–277. doi:10.1016/j.catena.2018.12.023

Deb, K., 2001. *Multi-objective optimization using evolutionary algorithms*. New York: John Wiley.

Delft Hydraulics, 2013. *SOBEK software user's manual*. Delft, The Netherlands: WL| Delft hydraulics.

DeMaria, M., et al., 2014. Is tropical cyclone intensity guidance improving? *Bulletin of the American Meteorological Society*, 95 (3), 387–398. doi:10.1175/BAMS-D-12-00240.1

Doong, D.J., et al., 2016. Development of a new generation of flood inundation maps—A case study of the coastal city of Tainan, Taiwan. *Water*, 8 (11), 521. doi:10.3390/w8110521

Drucker, H., et al., 1996. Support vector regression machines. *Advances in Neural Information Processing Systems*, 9, 155–161.

Fang, H.T., et al., 2019. A two-stage approach integrating SOM-and MOGA-SVM-based algorithms to forecast spatial-temporal groundwater level with meteorological factors. *Water Resources Management*, 33 (2), 797–818. doi:10.1007/s11269-018-2143-x

Hagan, M.T., Demuth, H.B., and Beale, M.H., 1996. *Neural network design*. Boston, MA: PWS Publishing.

Haykin, S., 1994. *Neural networks: a comprehensive foundation*. New York, NY: MacMillan.

Henonin, J., et al., 2013. Real-time urban flood forecasting and modelling–a state of the art. *Journal of Hydroinformatics*, 15 (3), 717–736. doi:10.2166/hydro.2013.132

Ho, S.Y., Shu, L.S., and Chen, J.H., 2004. Intelligent evolutionary algorithms for large parameter optimization problems. *IEEE Transactions on Evolutionary Computation*, 8 (6), 522–541. doi:10.1109/TEVC.2004.835176

Hou, T.H., Su, C.H., and Chang, H.Z., 2008. An integrated multi-objective immune algorithm for optimizing the wire bonding process of integrated circuits. *Journal of Intelligent Manufacturing*, 19 (3), 361–374. doi:10.1007/s10845-008-0088-2

Hsiao, L.F., et al., 2013. Ensemble forecasting of typhoon rainfall and floods over a mountainous watershed in Taiwan. *Journal of Hydrology*, 506, 55–68. doi:10.1016/j.jhydrol.2013.08.046

Hsiao, L.F., et al., 2015. Blending of global and regional analyses with a spatial filter: application to typhoon prediction over the western North Pacific Ocean. *Weather and Forecasting*, 30 (3), 754–770. doi:10.1175/WAF-D-14-00047.1

Huang, C.C., et al., 2019. Interdisciplinary application of numerical and machine-learning-based models to predict half-hourly suspended sediment concentrations during typhoons. *Journal of Hydrology*, 573, 661–675. doi:10.1016/j.jhydrol.2019.04.001

Jang, J.S., 1993. ANFIS: adaptive-network-based fuzzy inference system. *IEEE Transactions on Systems, Man, and Cybernetics*, 23 (3), 665–685. doi:10.1109/21.256541

Jhong, B.C., Wang, J.H., and Lin, G.F., 2016. Improving the long lead-time inundation forecasts using effective typhoon characteristics. *Water Resources Management*, 30 (12), 4247–4271. doi:10.1007/s11269-016-1418-3

Jhong, B.C., Wang, J.H., and Lin, G.F., 2017. An integrated two-stage support vector machine approach to forecast inundation maps during typhoons. *Journal of Hydrology*, 547, 236–252. doi:10.1016/j.jhydrol.2017.01.057

Kuntiyawichai, K., et al., 2011. Comparison of flood management options for the Yang River Basin, Thailand. *Irrigation and Drainage*, 60 (4), 526–543. doi:10.1002/ird.596

Lee, J.H., et al., 2020. Integrated flood forecasting and warning system against flash rainfall in the small-scaled urban stream. *Atmosphere*, 11 (9), 971. doi:10.3390/atmos11090971

Lin, G.F., et al., 2009. Effective forecasting of hourly typhoon rainfall using support vector machines. *Water Resources Research*, 45 (8). doi:10.1029/2009WR007911

Lin, G.F., Lin, H.Y., and Chou, Y.C., 2013. Development of a real-time regional-inundation forecasting model for the inundation warning system. *Journal of Hydroinformatics*, 15 (4), 1391–1407. doi:10.2166/hydro.2013.202

Lin, G.F. and Jhong, B.C., 2015. A real-time forecasting model for the spatial distribution of typhoon rainfall. *Journal of Hydrology*, 521, 302–313. doi:10.1016/j.jhydrol.2014.12.009

Liong, S.Y. and Sivapragasam, C., 2002. Flood stage forecasting with support vector machines 1. *JAWRA Journal of the American Water Resources Association*, 38 (1), 173–186. doi:10.1111/j.1752-1688.2002.tb01544.x

Mamdani, E.H., December 1974. Application of fuzzy algorithms for control of simple dynamic plant. *Proceedings of the Institution of Electrical Engineersd*, 121(12), 1585–1588. IET doi:10.1049/piee.1974.0328

Marinos, P.N., 1969. Fuzzy logic and its application to switching systems. *IEEE Transactions on Computers*, 100 (4), 343–348. doi:10.1109/T-C.1969.222662

Ouyang, H.T., 2017. Characteristics of recursive and non-recursive adaptive network-based fuzzy inference system models for the forecast of typhoon inundation levels. *International Journal of Environmental Science and Technology*, 14 (11), 2495–2506. doi:10.1007/s13762-017-1336-9

Pan, T.Y., et al., 2011. Hybrid neural networks in rainfall-inundation forecasting based on a synthetic potential inundation database. *Natural Hazards and Earth System Sciences*, 11 (3), 771. doi:10.5194/nhess-11-771-2011

Pan, T.Y., et al., 2012. Risk analysis for casualties of flood disaster: a case study of Tainan City. *Journal of Taiwan Agricultural Engineering*, 58 (4), 95–110.

Pan, T.Y., et al., 2014. Coupling typhoon rainfall forecasting with overland-flow modeling for early warning of inundation. *Natural Hazards*, 70 (3), 1763–1793. doi:10.1007/s11069-011-0061-9

Prinsen, G.F. and Becker, B.P.J., 2011. Application of SOBEK hydraulic surface water models in the Netherlands hydrological modelling instrument. *Irrigation and Drainage*, 60, 35–41. doi:10.1002/ird.665

René, J.R., et al., 2014. Assessing the potential for real-time urban flood forecasting based on a worldwide survey on data availability. *Urban Water Journal*, 11 (7), 573–583. doi:10.1080/1573062X.2013.795237

Rumelhart, D.E., Hinton, G.E., and Williams, R.J., 1986. Learning representations by back-propagating errors. *Nature*, 323 (6088), 533–536. doi:10.1038/323533a0

Shen, H.Y. and Chang, L.C., 2013. Online multistep-ahead inundation depth forecasts by recurrent NARX networks. *Hydrology and Earth System Sciences*, 17 (3), 935–945. doi:10.5194/hess-17-935-2013

Tabari, H., et al., 2012. SVM, ANFIS, regression and climate based models for reference evapotranspiration modeling using limited climatic data in a semi-arid highland environment. *Journal of Hydrology*, 444, 78–89. doi:10.1016/j.jhydrol.2012.04.007

Teng, H.F., et al., 2020. Dependence of probabilistic quantitative precipitation forecast performance on typhoon characteristics and forecast track error in Taiwan. *Weather and Forecasting*, 35 (2), 585–607. doi:10.1175/WAF-D-19-0175.1

Tsai, Y.F., Chan, C.H., and Chang, C.H., 2015. Setting up the critical rainfall line for debris flows via support vector machines. *Natural Hazards and Earth System Sciences Discussions*, 3 (10), 5957–5975.

Vapnik, V., 1995. *The nature of statistical learning theory*. New York: Springer.

Vapnik, V., Golowich, S.E., and Smola, A.J., 1996. Support vector method for function approximation, regression estimation and signal processing. In: M.C. Mozer, M. Jordan and T. Petsche eds. *Advances in Neural Information Processing Systems*, 9, 281–287.

Versini, P.A., 2012. Use of radar rainfall estimates and forecasts to prevent flash flood in real time by using a road inundation warning system. *Journal of Hydrology*, 416, 157–170. doi:10.1016/j.jhydrol.2011.11.048

Verwey, A., et al., 2008. Implementing an urban rainfall-runoff concept in SOBEK for a Catchment in Singapore. In: *Proceedings of water down under 2008*, Singapore., 36.

Wu, C.L., Chau, K.W., and Li, Y.S., 2008. River stage prediction based on a distributed support vector regression. *Journal of Hydrology*, 358 (1–2), 96–111. doi:10.1016/j.jhydrol.2008.05.028

Yadav, A. and Satyannarayana, P., 2020. Multi-objective genetic algorithm optimization of artificial neural network for estimating suspended sediment yield in Mahanadi River basin, India. *International Journal of River Basin Management*, 18 (2), 207–215. doi:10.1080/15715124.2019.1705317

Yang, S.Y., et al., 2018. The damage assessment of flood risk transfer effect on surrounding areas arising from the land development in Tainan, Taiwan. *Water*, 10 (4), 473. doi:10.3390/w10040473

Yoon, S.S., 2019. Adaptive blending method of radar-based and numerical weather prediction QPFs for urban flood forecasting. *Remote Sensing*, 11 (6), 642. doi:10.3390/rs11060642

Yu, P.S., Chen, S.T., and Chang, I.F., 2006. Support vector regression for real-time flood stage forecasting. *Journal of Hydrology*, 328 (3–4), 704–716. doi:10.1016/j.jhydrol.2006.01.021